Rochester Institute of Technology

RIT Digital Institutional Repository

Theses

8-2015

Doping Profile Measurements in Silicon Using Terahertz Domain Spectroscopy (THz-TDS) Via Electrochemical Anodic Oxidation

Gaurav Tulsyan

Follow this and additional works at: https://repository.rit.edu/theses

Recommended Citation

Tulsyan, Gaurav, "Doping Profile Measurements in Silicon Using Terahertz Domain Spectroscopy (THz-TDS) Via Electrochemical Anodic Oxidation" (2015). Thesis. Rochester Institute of Technology. Accessed from

This Thesis is brought to you for free and open access by the RIT Libraries. For more information, please contact repository@rit.edu.

R.I.T

DOPING PROFILE MEASUREMENTS IN SILICON USING TERAHERTZ TIME DOMAIN SPECTROSCOPY (THz-TDS) VIA ELECTROCHEMICAL ANODIC OXIDATION

Gaurav Tulsyan
B.E. Metallurgical Engineering
Punjab Engineering College, Chandigarh, India

A thesis submitted in partial fulfillment of the requirements for the degree of Master of Science in Materials Science and Engineering in the School of Chemistry and Materials Science, College of Science

Rochester Institute of Technology
Rochester, NY
August 2015

Signature of the Author ____

Date

SCHOOL OF CHEMISTRY AND MATERIALS SCIENCE
COLLEGE OF SCIENCE
ROCHESTER INSTITUTE OF TECHNOLOGY
ROCHESTER, NEW YORK

CERTIFICATE OF APPROVAL

M.S. DEGREE THESIS

The M.S. Degree Thesis of Gaurav Tulsyan has
been examined and approved by the thesis
committee as satisfactory for the thesis required for
the Master's degree in Materials Science and Engineering.

____

Dr. Christiaan P Richter, Thesis Advisor

____

Dr. Shu Chang, Committee Member

____

Dr. Carlos A Diaz, Committee Member

____

Dr. Stefan Preble, Committee Member

____

Date

ABSTRACT

Doping profiles are engineered to manipulate device properties and to determine electrical performances of microelectronic devices frequently. To support engineering studies afterward, essential information is usually required from physically characterized doping profiles.

Secondary Ion Mass Spectrometry (SIMS), Spreading Resistance Profiling (SRP) and Electrochemical Capacitance Voltage (ECV) profiling are standard techniques for now to map profile. SIMS yields a chemical doping profile via ion sputtering process and owns a better resolution, whereas ECV and SRP produce an electrical doping profile detecting free carriers in microelectronic devices. The major difference between electrical and chemical doping profiles is at heavily doped regions greater than 10^{20} atoms/cm^3. At the profile region over the solubility limit, inactive dopants induce a flat plateau and detected by electrical measurements only. Destructive techniques are usually designed as stand-alone systems to study impurities. For an in-situ process control purpose, non-contact methods, such as ellipsometry and non-contact capacitance voltage (CV) techniques are current under development.

In this theses work, terahertz time domain spectroscopy (THz-TDS) is utilized to achieve electrical doping profile in both destructive and non-contact manners. In recent years the Terahertz group at Rochester Institute Technology developed several techniques that use terahertz pulses to non-destructively map doping profiles. In this thesis, we study a destructive but potentially higher resolution version of the terahertz based approach to map the profile of *activated* dopants and augment the non-destructive approaches already developed. The basic idea of the profile mapping approach developed in this MS thesis is to anodize, and thus oxidize to silicon dioxide, thin layers (down to below 10 nm) of the wafer with the doping profile to be mapped. Since the dopants atoms and any free carriers in the silicon oxide thin film are invisible to the terahertz probe this anodization step very effectively removes a ‘thin slice’ from the doping profile to be mapped. By iterating between anodization and terahertz measurements that detect only the ‘remaining’ non-

oxidized portion of the doping profile one can re-construct the doping profile with significantly higher precision compared to what is possible by only a single non-destructive measurement of the un-anodized profile as used in the non-destructive version of our technique.

In this MS thesis we explore all aspects of this anodization based variation of doping profile mapping using free space terahertz pulses. This includes a study of silicon dioxide thin film growth using a room temperature electrochemical oxidation process. Etching procedures providing the option to remove between successive anodization and terahertz measurement steps. THz-TDS measurements of successively anodized profiles will be compared with sheet resistance and SIMS measurements to benchmark and improve the new technique.

ACKNOWLEDGEMENTS

First and foremost, I would like to express my sincerest gratitude to my advisor Dr. Christiaan Richter for taking me in his group, for his valuable guidance and being generous throughout my research and graduate studies at RIT. I truly admire his passion for research. His open mindedness and always ready to discuss attitude “why?” inspire me. I’m very thankful for all the opportunities he provided me in the Terahertz spectroscopy nanomaterials lab.

I would also like to thank Dr. Stefan Preble for serving on my committee, sharing his lab space for THz-TDS setup and always being nice to me. I would also like to express thanks to Dr. Carlos A Diaz and Dr. Shu Chang for serving on my committee for their professional guidance and valuable inputs. I would also like to thank Dr. John Andersen, who taught me Solid State Science and always ready to answer and discuss my silly questions about fundamental science.

I would like to thank my group members, Dr. Chih Yu Jen, Thomas Close Jr., and Brendan McNamara. I would express my gratitude to Chih Yu for helping me with THz-TDS setup and explained the minute details regarding it.

I would also like to thank Dr. Paul Craig, head of School of Chemistry and Material Science (SCMS) and Dr. KSV Santhanam, former director of material science and engineering program. Thanks to SMFL and SCMS staff (Special thanks to both Autumn and Brenda).

Finally, I would like to thank my parents for having faith in me and allowed me to continue my studies in material science and engineering. I would deeply appreciate my elder brother Ankit’s motivating attitude for higher studies and his affection towards me. I would also like to thank Amit Khare for being a part of my journey in USA. Above all the almighty GOD who has been always with me at every stage of life.

TABLE OF CONTENTS

ABSTRACT iii
ACKNOWLEDGEMENTS v
TABLE OF CONTENTS vi
LIST OF FIGURES viii
LIST OF TABLES x
Chapter 1: Introduction 1
1.1 T-rays – Brief Introduction 1
1.2 Research Motivation 4
1.3 Summary of other standard existent techniques 5
1.4 THz-Spectroscopy system – operating principle 9
1.5 THz Applications 12
Chapter 2: Background and theory 14
2.1 Literature review of applications of THz techniques 14
2.2 Generation and detection of T-rays 15
2.2.1 THz Sources 15
2.2.2 THz Detectors 17
2.3 Physical theories: Complex refractive index, dielectric constant and conductivity 18
2.3.1 Drude-Lorentz Model 19
2.3.2 Transfer Matrix model 20
2.4 Equation for the calculation of complex THz transmission 22
Chapter 3: Brief Overview: Silicon doping 24
3.1 Fundamentals of doping in semiconductors 24
3.2 Intrinsic semiconductors 25
3.3 Extrinsic semiconductors 26
3.4 Ion implantation Technology 27
3.4.1 Process parameters for ion implantation [65] 27
Chapter 4: Electrochemical Anodic Oxidation 31

4.1 Silicon dioxide thin films 31
4.2 Experimental set up 32
4.3 Study of SiO_2 growth electrochemically and influences of other parameters . 33
4.4 Sample preparation 35
Chapter 5: Results 38
5.1 THz measurements in time domain 38
5.2 Demonstration of reverse mapping of doping profile 39
5.3 Experimental and theoretical results 42
5.4 Doping profile using sheet resistance (Irvin's curve) 46
5.5 Benchmark and comparison 47
Conclusion 48
References 51
Appendix 57
A. Flow chart illustrating new concept 57
B. Derivation of complex transmission equation 58

LIST OF FIGURES

Figure 1.1 The electromagnetic spectrum 2

Figure 1.2 Absorption coefficients of phosphorous doped (10^{18} cm^{-3}) silicon and lightly doped (10^{15} cm^{-3}) silicon covering electromagnetic spectrum from the microwave to the visible. This plot clearly explains why THz is optimal spectral window for silicon for metrology purpose. SiO_2 refers to silica clusters and 'ph' represents phonons [15] 3

Figure 1.3 The difference of free carrier absorption in two spectra of silicon for two different doping 10^{15} cm^{-3} and 10^{18} cm^{-3} as a function of wavelength. Note that the free carrier absorption is very weak above THz frequencies. At lower frequencies (< 0.1 THz), there is free carrier absorption, however the dispersion is negligible relative to THz frequencies [15] 4

Figure 1.4 Standard characterization techniques to measure the doping profiles [15] 7

Figure 1.5 (a.) THz-TDS experimental setup (b.) Operating principle for generating the THz radiation 11

Figure 2.1 Brief summary of THz techniques history [15] 14

Figure 2.2 Illustration of transmission and reflection of light in a single dielectric layer 20

Figure 2.3 The new derived equation to calculate THz transmission for the first two peak in time domain 23

Figure 3.1 Representation of p-type silicon (boron doped) and n-type silicon (phosphorous doped) 26

Figure 3.2 Projected range (R_p) for some common dopants in silicon [65] 29

Figure 3.3 Definition of tilt and twist angle for the ion beam [65] 30

Figure 4.1 Electrochemical anodic oxidation set up 33

Figure 4.2 Silicon oxide thin film growth study with voltage 33

Figure 4.3 Study of silicon oxide growth with time at 100 V and 120 V 35

Figure 4.4 SIMS profile of the sample and sheet resistance measurements with respect to etched silicon 36

Figure 5.1 Time domain measurements of silicon samples 39

Figure 5.2 Demonstration of reverse mapping via destructive way 40

Figure 5.3 Both experimental and predicted results (spectra and reverse doping profile) 46
Figure 5.4 Doping profile presentation using SIMS, sheet resistance and our method (THz-TDS).. 47

LIST OF TABLES

Table 3.1 Parameters of common doping in silicon [65]... 28

Chapter 1: Introduction

1.1 T-rays: Brief overview

Terahertz (THz) radiation (T-rays) as shown in figure 1.1, lies in frequency gap of the infrared and microwaves region of the electromagnetic spectrum, typically referred the frequencies from 0.1 THz to 30 THz (1 THz = 10^{12} cycles per second). Historically, the major use of THz spectroscopy has been by chemists and astronomers in the spectral characterization of the rotational and vibrational resonances and thermal emission lines of simple molecules due to low photon energies and long wavelengths [1, 2]. The background noise (which is room temperature energy i.e. 25 meV at 6 THz) resulted from incoherent light limits the generation and detection of THz rays to implement this technique in earlier days. The first prototype of THz system was developed in 1985 and used for scientific purposes as described in chapter 2. These days the THz technology is being used in wide variety of applications such as, information and communications technology (ICT), biological and medical sciences [3-6], non-destructive evaluation, homeland security [7-9], quality control of food and agricultural products [10,11], global environmental monitoring and ultrafast computing etc. [12].

Development of THz-TDS, THz imaging & high power THz generation by non-linear effects are the few breakthroughs to push the THz research into the center stage. These tools are proven to be far superior to analyzing wide variety of materials than the conventional tools.

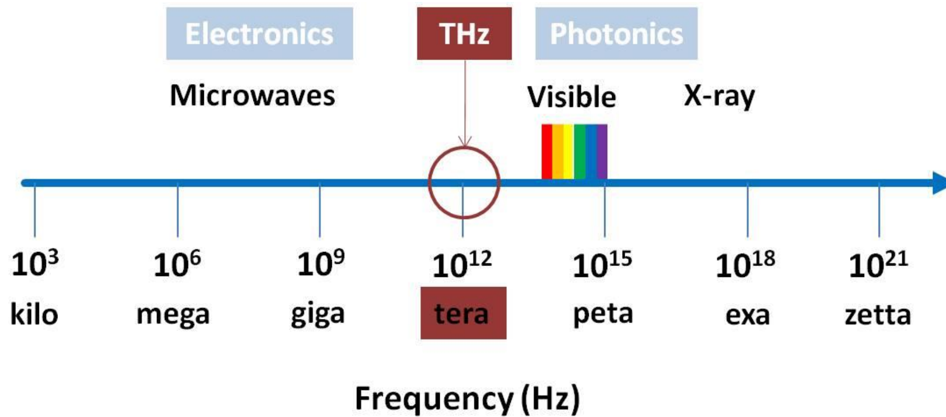

Figure 1.1 The electromagnetic spectrum.

Electromagnetic spectrum of free carrier absorptions for two doping level is shown in figure 1.2. THz spectroscopy is having advantages over microwave detected photo conductance decay (μW-PCD) [13] and Fourier transform infrared spectroscopy (FTIR) [14], which lies in between microwave and infrared regions respectively. In MIR (Mid-Infrared), NIR (Near Infra-red) and visible regions, photons have large energy to see the features like impurity absorption, phonon or inter-band transitions, thus difficult to study the behavior of free carriers in these regions. For example, FTIR is generally used to study molecular vibrations and impurity absorption. Lower frequencies in the far infrared range, namely microwave and terahertz emphasize the behavior of free carriers and sometimes phonons and allow studying these features.

This research aims to study the free carriers in silicon using THz wavelengths and utilize it to develop a metrology to map the doping profile via a destructive technique of anodic oxidation. The same method can be utilized to study free carriers in other semiconductor materials as well.

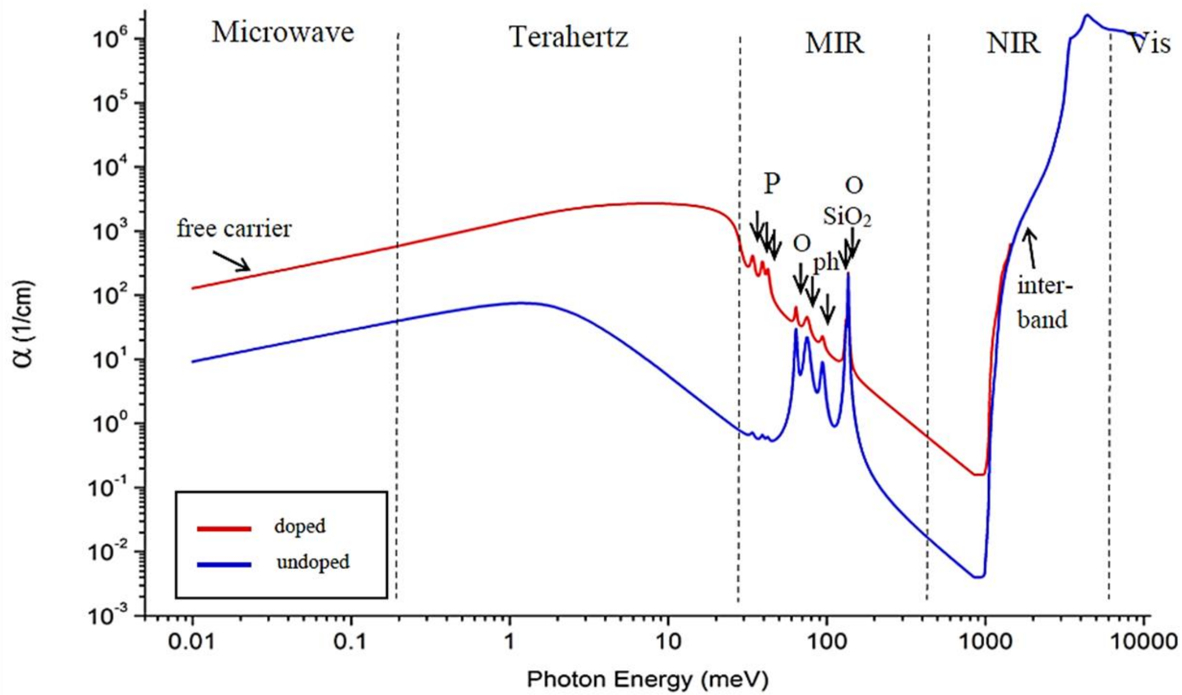

Figure 1.2 Absorption coefficients of phosphorous heavily doped (10^{18} cm^{-3}) silicon and lightly doped (10^{15} cm^{-3}) silicon covering electromagnetic spectrum from the microwave to the visible. This plot clearly explains why THz is optimal spectral window for silicon for metrology purpose. SiO_2 refers to silica clusters and 'ph' represents phonons [15].

Microwave region photons have low energy; so, THz frequencies play a pivotal role to study pure behavior of free electrons. Figure 1.3 shows the susceptibility of the free carrier absorption between moderately doped (10^{18} cm^{-3}) and lightly doped silicon (10^{15} cm^{-3}) [15]. From figure 1.2, there is virtually no contrast in the spectra except the absorption for these two doping level (therefore sensitivity to doping levels can be detected), however excellent contrast in the THz range and low to moderate contrast in microwave range. The slope of this plot (i.e. dispersion) even matters more, the dispersion is of critical importance for a metrology of the kind proposed here since it is the differences in the transmittance, reflectance, absorbance and phase delay of different adjacent frequencies (in a single broadband pulse) through the specimen. These likely features make THz-TDS an excellent metrology tool to monitor the electrical performance of the device that can be potentially utilized as inline process control in the semiconductor

fabrication processes. Comparing with methods μW-PCD, which provides the single frequency information, THz spectrum contains the multiple frequency information, which could potentially be used for complicated applications.

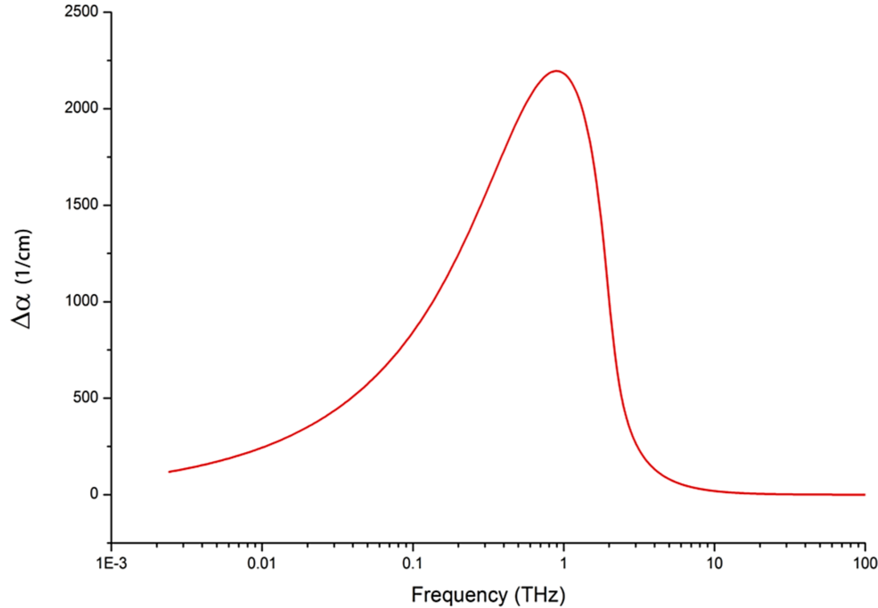

Figure 1.3 The difference of free carrier absorption in two spectra of silicon for two different doping 10^{15} cm^{-3} and 10^{18} cm^{-3} as a function of wavelength. Note that the free carrier absorption is very weak above THz frequencies. At lower frequencies (< 0.1 THz), there is free carrier absorption, however the dispersion is negligible relative to THz frequencies [15].

1.2 Research Motivation

The motivation of thesis is to design a metrology to predict the electrical doping profiles in semiconductor devices utilizing the outstanding information hidden in THz frequencies. These days mainstream characterization techniques to map doping profiles are designed as stand-alone systems, due to which it is difficult to have feedback measurements in a timely manner. This THz-TDS system enables us to consider a virtually non-contact option. In 2012 the USA photovoltaic Manufacturing Consortium (PVMC) embarked on a campaign with 38 separate organizations from industries, labs and academia to identify and prioritize the critical challenges

in c-Si (crystalline silicon) metrology. One of the key challenges in the cell production metrology challenges is “High-throughput evaluation of emitter doping process (e.g., doping uniformity, resistivity mapping, junction depth, measuring doping profile on a textured surface)”. SIMS (Secondary Mass Ion Spectrometry) [16, 17], SRP (Spreading Resistance profiling) [18, 19] and ECV (Electrochemical Capacitance Voltage) [20, 21] are widely used standard techniques in industries to determine doping profile, however these could not fulfill the high-throughput assessment so far. Differ from these techniques; THz-TDS, the only broadband technique utilized as an optical metrology to attain doping profile with few advantages as below [15]:

- Non-contact (due to optical method)
- High sensitivity to carrier concentrations
- High resolution
- Measures both amplitude and phase shift and additional information (mobility, lifetime of carriers etc.)
- Measure rapidly with high accuracy

Non-contact metrology tools would open the new excited area to increase the throughput production through *in-situ* process control with real-time feedback in industries. Therefore, THz technique motivates us to develop an alternative metrology to map doping profile for the inline process monitor purpose.

1.3 Summary of other existent standard techniques

For the realization of semiconductor devices of optimum performance and reliability the accurate knowledge of the doping profile is indispensable. For comprehensive characterization, not only the dopant distribution but also the concentration of free carriers must be determined.

Carrier profiling in connection with dopant profiling provides information about the electrical activity of impurities.

Figure 1.4 briefly describes the common existent techniques to determine doping profiles. The most reliable high resolution technique is SIMS, a destructive way, however widely used in semiconductor industries for doping profile measurement. Its popularity stems from unparalled sensitivity (down to *ppb,* parts per billion levels) and its potential to detect all species of interest. The results are quite encouraging in that the depth scale can be determined within a precision of 10% and the concentration scale (provided an appropriate standard is available) within 15%. This is quite expensive, slow and gives chemical doping profile as opposed to electrical one.

Spreading Resistance Profiling (SRP) or Spreading Resistance Analysis (SRA) [22] analyzes resistivity vs depth (surface carrier concentration vs depth) in semiconductors. This method provides the electrically active doping profile as compared to chemical doping profile similar to SIMS. Electrical characterization of dopant profiles forms an essential part of this process. SRP is in principle a very simple method, which determines the resistance between two tips on a beveled surface. This process is repeated when the tips are stepping down the bevel such that ultimately the spreading resistance as function of depth is obtained. The inherent geometrical resolution is determined by the step size of the probe tips (1-2.5 μm), and the magnification provided by the small bevel. SRP is limited to silicon and few other semiconductor materials, whereas SIMS can profile the atomic concentration of almost anything. Relative to SIMS, SRP provides less spatial resolution therefore more convenient for deeper junctions. The attractiveness of SRP is that it provides unchallenged sensitivity (down to the 10^{11} level) for every dopant which is electrically active. Tan et al [23] has published the work of measuring ultra-shallow junction of 121 nm using SRP and obtained a reasonable agreement

with the result from SIMS. For deep profiles the technique is well established and good agreement with SIMS. However, for shallow carrier profiles the situation becomes more critical. In applications toward very shallow profiles, SRP always produces junction depths shallower compared with SIMS. SRP is limited if junctions less than 100 nm deep are to be characterized. In addition, the proper application of improved experimental techniques for sample preparation and probe conditioning in connection with an advanced analysis of the measured raw data is required in order to obtain reliable results by SRP.

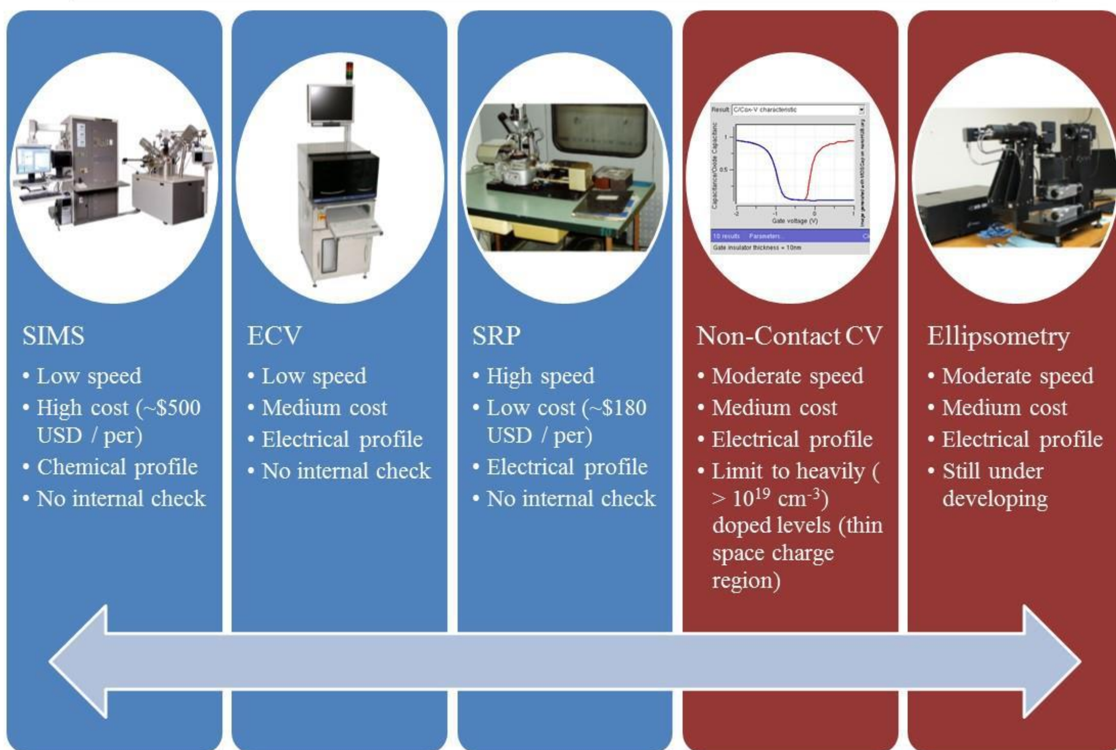

Figure 1.4 Standard characterization techniques to measure the doping profiles [15].

One of the major limitations of SRP is its sensitivity to probe conditioning and the need for calibrating the probe contact. An elegant and alternative method which does provide quantitative results is the capacitance-voltage technique (C-V) [22]. The method relies on the fact that the width W of a reverse biased region is proportional to the applied bias V. In Capacitance Voltage (CV) measurement, a metal-semiconductor (Schottky) junction is formed

with the sample and capacitance is measured at various voltages to infer the substrate properties using theoretical model (Shockley or depletion approximation model [24]) together with empirical correction factors. Profiles based on this method are acceptable for sufficiently shallow junctions. As voltage is used to measure capacitance, the heavily doped regions (usually > 10^{19} cm^{-3}) limit this technique due to a thin space charge region formed by applied voltage.

The ECV technique exploits this strength via cycling etching step with CV measurement in process. It is slow and destructive; still it is more accurate than the conventional capacitance voltage method. The electrochemical capacitance-voltage technique (ECV) is well established and widely used for carrier-concentration profiling of III/V semiconductors. The strengths of this method are simple sample preparation, direct correspondence of the measured magnitudes to concentration and depth, and virtually unlimited profiling depth. ECV is best suited for the characterization of shallow doping profiles. Therefore, this technique is particularly attractive for scaled-down devices in advanced IC technology.

The other technique is Ellipsometry (IR ellipsometry), which measures the doping profile as a non- contact and non-destructive way. An Ellipsometry technique is good at studying thin films such as anti-reflective coatings or passivation layers [25]. The existing UV-visible-near infrared ellipsometer have a significant disadvantage over the THz light as described in earlier section. Commercial FIR/THz ellipsometer doesn't exist, however Woollam Corporation and collaborators are trying to build the one [26, 27].

With respect to dopant profiling, secondary ion mass spectrometry (SIMS) is the most universal and sensitive technique with the potential to satisfy the criteria mentioned above. However, concern can be raised regarding the depth resolution and in particular regarding the quantification near the surface and in multilayer profiles.

Therefore, to measure electrically active doping profile, we have developed a new metrology which is non-contact, however destructive (electrochemical anodic oxidation) using THz-time domain spectroscopy in this theses research work.

1.4 THz Spectroscopy system (operating principle of THz-TDS)

Terahertz spectroscopy allows a material's far-infrared optical properties to be determined as a function of frequency. This information can provide an understanding of material characteristics for a wide range of applications. It can be designed, either as reflection mode or transmission mode. We have utilized transmission mode in this research. A typical THz-TDS setup is shown in figure 1.5 (a) based on photoconductive antenna to generate and detect THz radiation. The principle of THz-TDS starts with a femtosecond laser producing an optical pulse train (~250 fs, 835 nm) by a mode lock achieved Titanium-sapphire laser. As generated optical pulse divides into two paths. One part (Path A) reaches the THz emitter (i.e. photoconductive antenna, semiconductor wafer or nonlinear crystal), where the optical pulses are transformed into THz radiation (ultrashort electromagnetic pulses). The THz emitter is shown in figure 1.5 (b). These excited THz pulse is collimated by a high resistivity hemispherical silicon lens and travels in free space (purged with nitrogen or compressed air to decrease the humidity) before reflecting from a parabolic mirror. A couple of parabolic mirrors as shown in the diagram used to focus the THz waves onto an ultrafast terahertz detector (for example a low-temperature-grown GaAs photoconductive switch or an electro-optic crystal). The other part (Path B) of the pulse from beam splitter is also delivered onto the detector as a reference signal after passing through a delay stage. A sample holder is located for the reference and sample measurements between the two parabolic mirrors, which causes a time delay and a reduction in the THz pulses magnitude. The reference THz pulse is measured considering air as a reference or can be

measured without the sample (only substrate). We determine both magnitude and phase information of the spectra (the absorption and refractive index (and therefore σ) of the sample) without using Kramers-Kronig relations.

THz-TDS has a numerous advantages over incoherent techniques [28]:

(i) able to extract the complex optical properties (refractive index) of a material without doing theoretical calculations using Kramers-Kronig relationship;

(ii) capability of removing Fabry-Perot reflections in thick substrates by windowing the time-domain data;

(iii) the time-resolved photoconductivity on picoseconds time scales can be measured in a non-contact way;

(iv) the time-gated detection of THz pulses allows all spectrometer components to be used at room temperature,

(a).

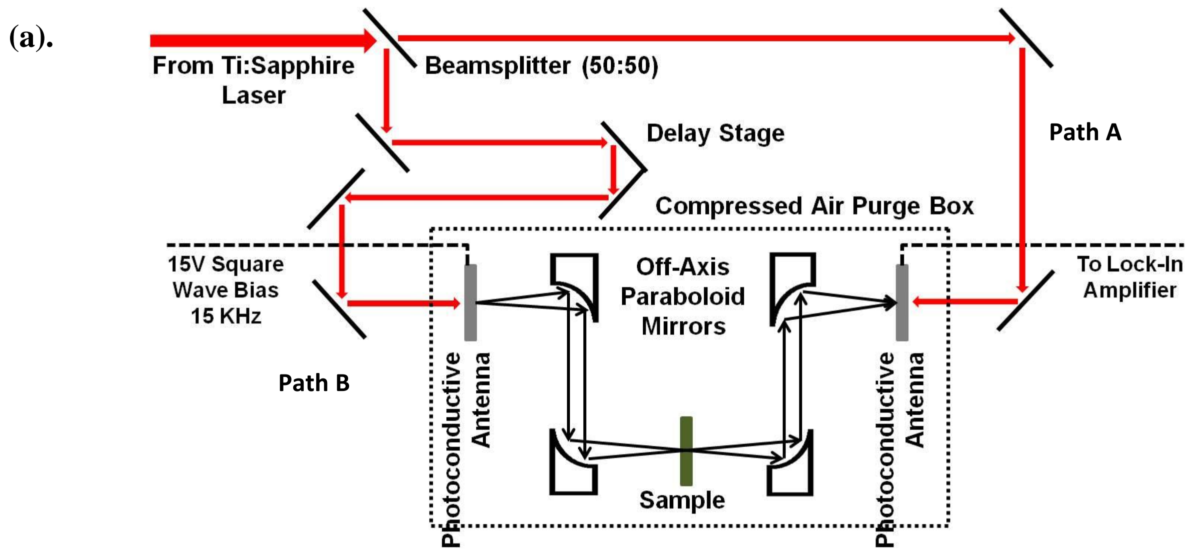

(b).

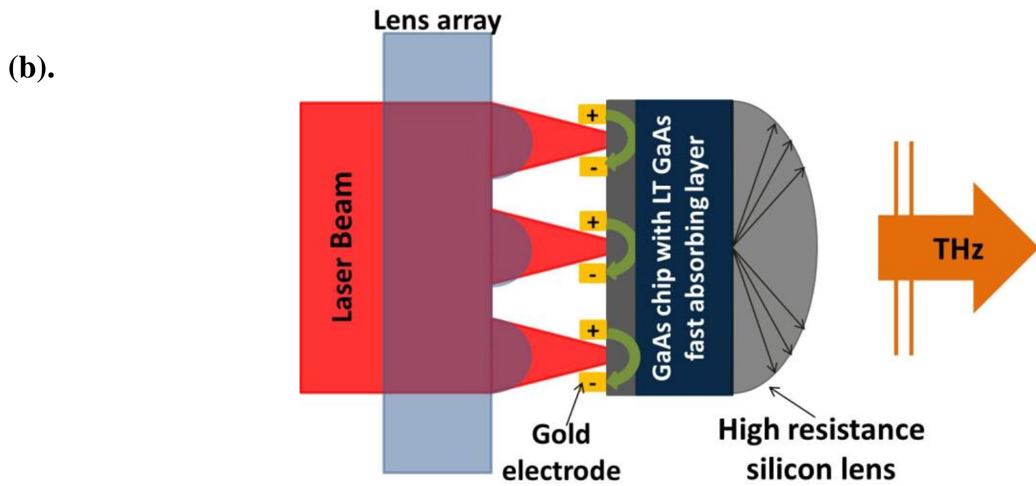

Figure 1.5 (a.) THz-TDS experimental setup. (b.) Operating principle for generating the THz radiation (Photoconductive Antenna).

However, there are disadvantages of the THz-TDS setup, which includes high cost of ultrafast laser. Apart from it, the bandwidth is not as broad as the commercially available FTIR. The other drawback includes the position of reference mirror which needs to be precisely determined to avoid phase errors to calculate optical properties [29, 30].

1.5 THz Applications

THz imaging has wide range of practical applications [31-36]. THz waves transmit through various materials that block light, however THz gives higher imaging resolution than microwaves. The THz beam can be focused using lens or mirrors to obtain the images by scanning the beam. The imaging resolution is defined by the THz beam diameter. Higher-frequency components need for better imaging resolution, but still not adequate for nanoscale applications.

There are lots of examples of materials evaluation; including inspection of silicon solar cells, nanocomposites, dielectric and polymer films [37-39]. THz TDS is already capable of evaluating various semiconductor wafer properties (few are described in this theses), such as mobility, wafer thickness, conductivity, carrier density etc. [40, 41]. THz imaging has also been used to inspect the space shuttle foam insulation as a non-destructive evaluation method. Due to THz sensitivity to moisture, this feature could be used to monitor water content in vegetables and fruits.

Almost all explosive and narcotic have a distinct feature in their THz spectra, allowing THz spectroscopy useful for security applications. These signatures allow the identification of many chemicals in a non-destructive way via their transmission spectra. Concisely, it is likely to distinguish illegal drugs and explosives using THz-TDS. As waves below 3.0 THz (wavenumber 100 cm^{-1}) can normally pass through envelopes, which allows to identify materials inside the mail without having to open it through THz multispectral images and component spatial-pattern analysis [42].

Experiments with optical-pump THz-probe systems reveal additional information (carrier dynamics) about materials [15]. An ultrafast optical pulse (visible light) is used to excite the

materials, followed by THz pulse to probe the dynamic far-infrared optical properties of the materials. Leitenstorfer *et al*. used an optical-pump THz-probe system to study and identify the charge-charge interactions in electron-hole plasma excited in gallium arsenide (GaAs) semiconductor material. This study provides experimental evidence to quantum-kinetic theoretical predictions about charge build-up particles [43].

Chapter 2: Background and theory

2.1 Literature review of applications of THz techniques

We briefly describe the history of terahertz spectroscopy as depicted in figure 2.1. The experimental physics of generating and detecting broadband THz pulses started with the discovery of the Austin switch in 70's [44] and developing in new directions like air plasma generation [45]. In 1985, the first THz spectroscopy set up was designed and implemented in diversified research areas as described earlier in chapter 1. Z-omega designed and developed first commercial THz-TDS and brought into the market through continuous technology innovation.

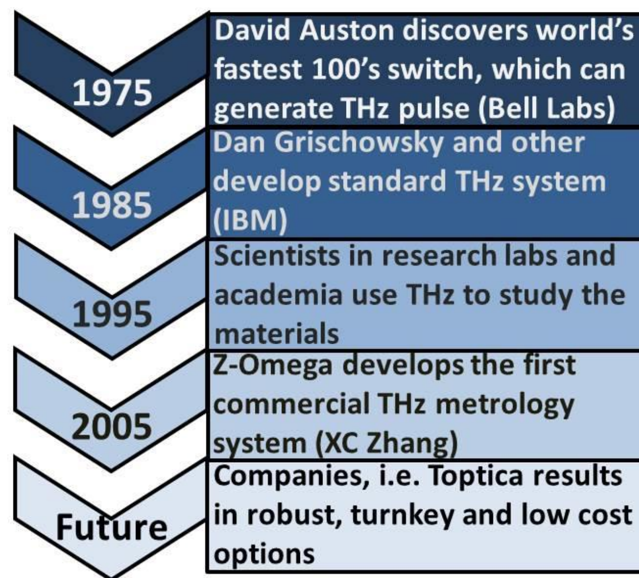

Figure 2.1 Brief summary of THz techniques history [15]

Relative to THz-TDS, the TRTS (Time Resolved Terahertz Spectroscopy) is used to study transient carrier dynamics in materials by measuring up to sub picosecond level, which allows studying fundamental science using TRTS. Few examples include such as studying bulk semiconductors, semiconductor heterostructures, superconductors, polymer-fullerene

heterojunctions, dye sensitized nanoparticles and more [46]. In this work, we have utilized transmission mode THz-TDS to study the free carriers in silicon.

Development of THz time-domain spectroscopy (THz-TDS), THz imaging, and high power THz generation by means of nonlinear effects are the few major breakthroughs, which have brought THz research into the center stage. THz techniques are far better than to conventional tools for studying and examining a wide variety of materials and have better resolution than any other methods.

Photonics has played a key role to the realization of various important THz devices like the development of the quantum cascade laser (QCL) which provides a powerful continuous wave (c.w.) THz source and the uni-travelling-carrier photodiode (UTC-PD) uses a photomixing technique to produce sub-THz waves for applications such as wireless communication [47].

Moreover, recent advances in high frequency electronics performance have also furthered terahertz technology. Semiconductor and superconductor logic circuits are already been operating at higher frequencies than 0.1 THz (100 GHz). Recently developed solid state electronic devices for example resonant tunnelling diodes and THz single-photon detectors, as well as the conventional Schottky barrier diodes (SBDs), continue to move into the THz frequencies at the same time [47].

2.2 Generation and detection of T-rays

2.2.1 THz Sources

THz sources may be classified as incoherent thermal sources, broadband pulsed techniques or narrowband continuous-wave methods [47].

(a.) Broadband THz Sources

Most broadband pulsed terahertz (THz) sources are designed on the excitation of semiconductor materials with ultrashort pulses. Numerous mechanisms have been developed to generate THz radiation, including plasma oscillations, photocarrier acceleration in photoconducting antennas, electronic non-linear transmission lines, and second-order non-linear effects in electro-optic crystals [47]. The conversion efficiencies is quite low in all of these sources, and subsequently THz beam power tends to be in the micro watt region, whereas the femtosecond optical source average power is in the range of 1-2 Watts.

Optical rectification and Photoconduction are the widely used approaches to generate broadband pulsed THz beams. Few examples of photoconductors include high-resistivity GaAs, InP and radiation-damaged silicon wafers, whereas GaAs, ZnTe, and organic crystals such as the ionic salt DAST are the optical rectifiers. Metallic electrodes (i.e. gold) are used to bias the photoconductive gap and form an antenna.

The mechanism to generate THz waves in photoconductive antenna initiates by an ultrafast laser pulse (with a photon energy greater than the bandgap of the semiconductor material $h\nu \geq E_g$), creates e-h pairs in the photoconductors. Due to static bias field, the free carriers accelerate to generate a transient photocurrent in the photoconductor, and the fast, time varying current emits electromagnetic terahertz radiations. The resultant THz wave's intensity and bandwidth depends upon various materials properties. Rapid photocurrent rise and decay times are desirable to attain efficient THz radiation, therefore InAs and InP are attractive due to their small effective electron masses over other semiconductor materials. Other important material parameter include the maximum drift velocity, however is usually limited by the intraband scattering rate in direct gap semiconductors such as GaAs (Gallium Arsenide) [48,49]. The other factor is break down field of material, which determines the maximum bias that may

be applied. The radiating energy primarily comes from stored surface energy as static bias field, so terahertz energy scales up with the optical fluency and bias [50].

In another category, THz waves are generated by optical rectification (nonlinear optical effects), which is based on the inverse process of the electro-optic effect [51]. In a similar way like photoconduction, femtosecond laser pulses are needed, but in contrast to photoconducting which requires the optical beam as a trigger, the energy of pulsed THz radiation comes directly from the exciting laser pulse in optical rectification mechanism. The conversion efficiency mainly depends on phase matching conditions and the non-linear coefficient of material. This technique was first demonstrated using $LiNbO_3$ material for generating far infra light [52]. Optical rectification usually provides lower output power relative to photoconductive antennas, however it has the benefit of providing high bandwidths waves, up to 50 THz [53].

(b.) Narrowband THz sources

Narrow band THz sources are important for high-resolution spectroscopy applications. These sources have applications in telecommunications fields, high bandwidth intersatellite links etc. These sources mostly used for generating low-power (<100 microwatt) continuous-wave THz radiations. It is achieved through conversion of lower frequency microwave oscillators. Examples include such as dielectric-resonator oscillators and voltage-controlled oscillators. Upconversion is achieved through a series of planar GaAs Schottky-diode multipliers to get frequencies as high as approximately 3 THz [54].

2.2.2 Terahertz Detectors

THz detectors were studied in late 90's and nowadays low temperature grown gallium arsenide (GaAs) is often used as a photoconductive antenna. Electro-optic sampling methods are also available for time domain detection as an alternate approach of photoconductive antenna,

which can be used to measure over 100 THz using an ultrafast laser source (10-fs-laser) and a thin nonlinear crystal such as GaSe [55]. DTGS (deuterated triglycine sulphate) crystals, bolometers, SBDs and SIS (superconductor-insulator-superconductor) junctions are normally used as conventional THz detectors [56-58].

2.3 Physical theories: complex refractive index, dielectric constant and conductivity

The complex refractive index $\tilde{n} = n + i\kappa$ defines the expression for the transmission or reflectivity of a material. The real part of $\tilde{n}$, namely n, is the same as the normal refractive index defined $n = \frac{c}{v}$ and imaginary part κ is called the extinction coefficient and directly proportional to the absorption coefficient α of the medium as per Beer's law relationship $\alpha = \frac{2\kappa\omega}{c} = \frac{4\pi\kappa}{\lambda}$, where λ, is the free space wavelength of the light.

Defining refractive index from Maxwell's equations derivation,

$$\tilde{n} = \sqrt{\epsilon\mu}$$

where ϵ is dielectric function (or permittivity) which describes how easily an electric field penetrates the medium and the permeability μ details the magnetic response. The dielectric function is in general complex number, with an imaginary part ϵ_2 in spectral region with carrier absorption and defines as below

$$\tilde{\epsilon}(\omega) = \epsilon_1(\omega) + i\epsilon_2(\omega)$$

The corresponding conductivity σ of mobile charges is also a complex number and states as below,

$$\sigma(\omega) = \sigma_1(\omega) + i\sigma_2(\omega)$$

which describes conduction model and material properties. This expression is valid for a monochromatic plane wave propagating in the $\tilde{\boldsymbol{k}}$ direction, with a time dependent electric field of

the form $E(t) = E_0 e^{i(k.r-\omega t)}$. Varying these parameters provide the essential information to sketch the doping profile.

2.3.1 Drude-Lorentz Model

The simplest model of the frequency-dependent conductivity of metals and semiconductors is described by the Drude-Lorentz approach and was first proposed by Paul Drude to explain the transport properties of electrons in conductors in 1900 [59]. The major assumption of this model is that elastic scattering events occurs in a free electron sea with a complete momentum randomization, i.e. electron-hole plasma is considered as a non-interacting gas (independent of energy). Any long-range interactions between ions or electrons, between only electrons are neglected except instantaneous collisions. Both DC and AC conductivity are thus determined through following equation:

$$\sigma_0 = \frac{Ne^2\tau}{m_0} \tag{2.1}$$

$$\sigma(\omega) = \frac{\sigma_0}{1-i\omega\tau} = \frac{\sigma_0}{1+\omega^2\tau^2} + \frac{i\sigma_0\omega\tau}{1+\omega^2\tau^2} \tag{2.2}$$

where, N, e, τ, m_0 represent number of electrons per unit volume, electron charge $(1.6 * 10^{-19}\ C)$, scattering time and mass of electron.

The Drude response describes that the real component of the AC conductivity approaches to the maximum (DC, σ_0) and the imaginary part to $\frac{\sigma_0}{1-i}$, when radial frequency is inversely proportional to the scattering time τ. In metals, this characteristic frequency $\frac{1}{\tau}$ is in the infrared range. These responses are not to be found experimentally. For materials like doped semiconductors with a much lower frequencies $\frac{1}{\tau}$, frequency dependent conductivity closely follows the above relationship described in equation 2.2. When $E_{THz} > 4MVm^{-1}$, the THz pulse may accelerate electrons sufficiently to alter their scattering rates, making Drude model no

longer considerable. THz system available at RIT is having electric field less than the above value to avoid this case.

2.3.2 Transfer Matrix Method (section taken from "*Introduction to modern optics*" by G. R. Fowles)

Transfer matrix is normally used to describe the transmission and reflection behavior of light as a function of complex refractive index in multi-layer films. The transmitted and reflected wave vector and electric field of an incident light on a single dielectric layer of index n_1 and thickness of L is described in below figure 2.2. In the figure 2.2, E_0 is the amplitude of the electric vector of the incident beam (THz light); E'_0 is the reflected beam and E_T of the transmitted beam. E_1 and E'_1 are the electric field amplitudes of the forward and backward traveling waves, respectively, as shown in the figure 2.2.

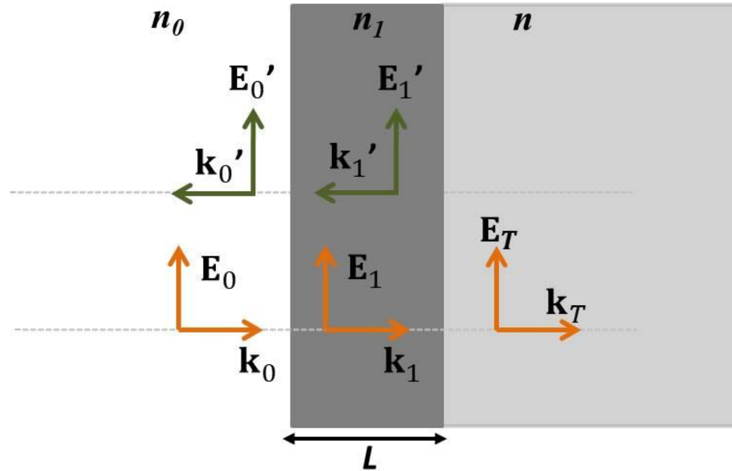

Figure 2.2 Illustration of transmission and reflection of light in a single dielectric layer.

Applying boundary conditions at both the interfaces separated by thickness L that requires electric field and magnetic fields to be continuous and eliminating amplitudes E_1 and E'_1, we obtain the following expression,

$$1 + \frac{E'_0}{E_0} = (\cos kl - i\frac{n}{n_1}\sin kl)\frac{E_T}{E_0} \tag{2.3}$$

Simplifying further, we get

$$n_0 - n_0 \frac{E_0'}{E_0} = (-i\, n_1 \sin kl + n \cos kl) \frac{E_T}{E_0} \tag{2.4}$$

Writing in matrix form, we get

$$\begin{bmatrix} 1 \\ n_0 \end{bmatrix} + \begin{bmatrix} 1 \\ -n_0 \end{bmatrix} \frac{E_0'}{E_0} = \begin{bmatrix} \cos kl & \frac{-i}{n_1} \sin kl \\ -in_1 \sin kl & \cos kl \end{bmatrix} \begin{bmatrix} 1 \\ n \end{bmatrix} \frac{E_T}{E_0} \tag{2.5}$$

This can be abbreviated as

$$\begin{bmatrix} 1 \\ n_0 \end{bmatrix} + \begin{bmatrix} 1 \\ -n_0 \end{bmatrix} r = M \begin{bmatrix} 1 \\ n \end{bmatrix} t$$

Here, “r” is reflection coefficient, which is

$$r = \frac{E_0'}{E_0}$$

and the “t” transmission coefficient,

$$t = \frac{E_T}{E_0}$$

The matrix

$$M = \begin{bmatrix} \cos kl & \frac{-i}{n_1} \sin kl \\ -in_1 \sin kl & \cos kl \end{bmatrix} \tag{2.6}$$

is called the transfer matrix. Here $= \frac{n_1 \omega}{c}$, a wave vectors which depends on the frequency and the refractive index of that layer. C is speed of light which is $3 \times 10^8 \frac{m}{s}$.

Now assuming we have N layers numbered $1,2,3,4, \dots \dots N$ having indices of refraction $n_1, n_2, n_3, n_4, \dots \dots n_N$ and thickness $l_1, l_2, l_3, l_4, \dots \dots l_N$ respectively. The reflection and transmission coefficients of the multilayer film are related by a similar matrix equation:

$$\begin{bmatrix} 1 \\ n_0 \end{bmatrix} + \begin{bmatrix} 1 \\ -n_0 \end{bmatrix} r = M_1 M_2 M_3 M_4 \dots \dots M_N \begin{bmatrix} 1 \\ n \end{bmatrix} t = M \begin{bmatrix} 1 \\ n \end{bmatrix} t \tag{2.7}$$

where the transfer matrices of the various layers are denoted by $M_1, M_2, M_3, M_4, \dots \dots M_N$. Each transfer matrix is in the form given by the equation (transfer matrix of the thin film) with appropriate values of n, l, k. The overall transfer matrix M is the product of the individual transfer matrices. Let the elements of M be A, B, C, D, that is

$$M_1 M_2 M_3 M_4 \dots \dots M_N = M = \begin{bmatrix} A & B \\ C & D \end{bmatrix}$$

solving equation 2.7 for r and t in terms of these elements, we achieve

$$r = \frac{An_0 + Bnn_0 - C - Dn}{An_0 + Bnn_0 + C + Dn}, \quad t = \frac{2n_0}{An_0 + Bnn_0 + C + Dn} \tag{2.8}$$

2.4 Equation for the calculation of complex THz transmission [15]

In our THz measurements, we do measurements in the time region of -10 ps to 35 ps (picoseconds), which includes the main peak and the first internal reflection peak. The equation described in section 2.3.3 calculates the transmission using infinite time range. Since we go up to only two peaks, a new equation should be introduced to calculate the THz transmission. The calculation is described in appendices. Here $\frac{\widetilde{E_{T_1}}}{\widetilde{E_0}}$ is the transmission from the main peak, where $\frac{\widetilde{E_{T_2}}}{\widetilde{E_0}}$ is the first internal reflection peak. $\widetilde{E_0}$ is assumed as the reference air scan.

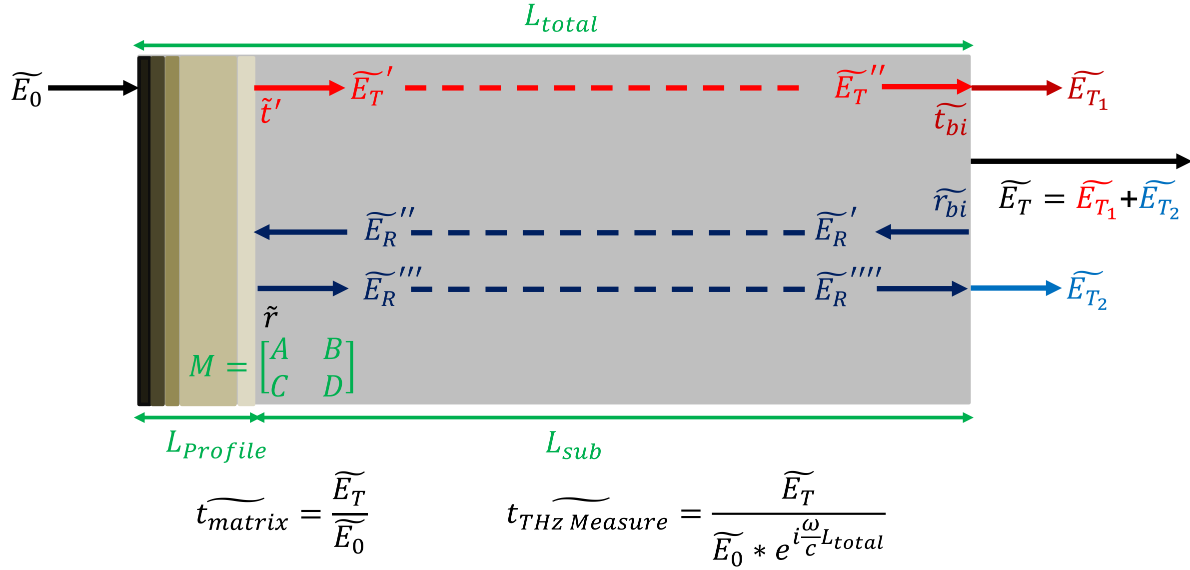

Figure 2.3 The new derived equation to calculate THz transmission for the first two peak in time domain.

$$\frac{\widetilde{E_{T_1}}}{\widetilde{E_0}} = \tilde{t}'\widetilde{t_{bi}}e^{i\frac{n_{sub}\omega}{c}L_{sub}} = \frac{2}{A + Bn_{sub} + C + Dn_{sub}}\frac{2n_{sub}}{n_{sub}+1}e^{i\frac{n_{sub}\omega}{c}L_{sub}}$$

$$\frac{\widetilde{E_{T_2}}}{\widetilde{E_0}} = \frac{2n_{sub}}{n_{sub}+1}\frac{An_{sub} + Bn_{sub} - C - D}{An_{sub} + Bn_{sub} + C + D}\frac{n_{sub}-1}{n_{sub}+1}\frac{2}{A + Bn_{sub} + C + Dn_{sub}}e^{i\frac{3n_{sub}\omega}{c}L_{sub}}$$

$$\frac{\widetilde{E_T}}{\widetilde{E_0}} = \frac{\widetilde{E_{T_1}}}{\widetilde{E_0}} + \frac{\widetilde{E_{T_2}}}{\widetilde{E_0}}$$

Chapter 3: Brief Overview: Semiconductor Doping

3.1 Fundamentals of Doping in Semiconductors (Silicon)

Doping plays a key role in all the electronic devices and the basic MOSFET parameters are affected by dopants distribution. It refers to the process of introducing impurity atoms in a controlled way in order to define the electrical properties in semiconductor materials (usually III and V group species). The donors and acceptors doping modify the electron and hole concentration from 10^{13} up to 10^{21} cm^{-3}. The carrier concentration can also be spatially distributed fairly to create pn-junctions and produce built-in electric fields. Mostly semiconductor devices incorporate impurities (dopants) as a crucial ingredient to modify the electronic, optical characteristics and device structure.

Ion implantation is the extensively used technology to introduce dopants into a semiconductor material to form integrated circuits and devices [60, 61]. This relatively low temperature process uses ionized dopants, accelerated to high energies by electric fields and directed into the wafer at particular angle. The main reason to use this technique is precise and control the doping in wafer. Dopants can be masked either by any material which is thick enough to stop the implant ions or by self-aligned implants. After the implantation process, semiconductor's crystal structure is impaired by the implanted ions and the dopants are electrically inactive, since these are not part of the crystal lattice (occurs in majority of cases). A subsequent thermal annealing is needed to activate the dopants and to remove the produced crystal defects.

The initial material used for the fabrication of devices is monocrystalline silicon. Silicon wafers are produced either by the floating-zone crystal growth technique or by the Czochralski

crystal pull method [62]. Dopants are added to the molten silicon during the growth process in order to achieve the certain resistivity of the wafers in the range from 1 ohm-cm to 30 ohm-cm. Silicon wafers with a (100) surface plane are normally considered in semiconductor manufacturing, because the silicon-silicon dioxide (Si/SiO_2) interface provides the lowest defect density for this silicon [63]. At zero temperature, pure semiconductor material does not show any conductivity, as the vacant conduction band is separated by an energy gap E_g from the filled valence band. As the temperature is raised, electrons get thermal energy to move from the valence band to the conduction band. Electrons in the conduction band and holes in the valence band (the vacant orbitals) contribute to the electrical conductivity.

3.2 Intrinsic Semiconductor

An intrinsic semiconductor contains a negligibly small quantity of impurities relative to thermally generated electron and holes. The energy distribution of electrons in solids is given by the Fermi-Dirac statistics [64]. The Fermi-Dirac distribution is used to define the probability of an electronic state at energy E occupied by an electron in thermal equilibrium given by

$$f(E) = \frac{1}{1 + \exp\left(\frac{E - E_F}{k_B T}\right)} \tag{3.1}$$

The Fermi energy (E_F), the energy at which the probability of electron occupancy is exactly one-half. The probability of not finding an electron at energy E, $1\text{-}f(E)$, i.e. the probability of finding a vacancy (hole) there. At absolute T=0K, all the states below the Fermi level ($E<E_f$) are filled, i.e. $f(E)=1$ and all the states above the Fermi level ($E>E_f$) are empty, i.e. $f(E)=0$. At finite temperatures, continuous thermal agitation provides energy to excite electrons from the valence band to the conduction band and results in equal numbers of holes left in the valence band.

3.3 Extrinsic Semiconductor (Donors and Acceptors)

In modern semiconductor devices, doping refers to the process of introducing impurity atoms to define type and number of free carriers into a semiconductor material and can be directed by an external applied voltage. The electrical properties of a doped semiconductor are usually described by either the band model or the bond model. The semiconductor becomes extrinsic and impurity energy levels are generated when a semiconductor is doped with impurities.

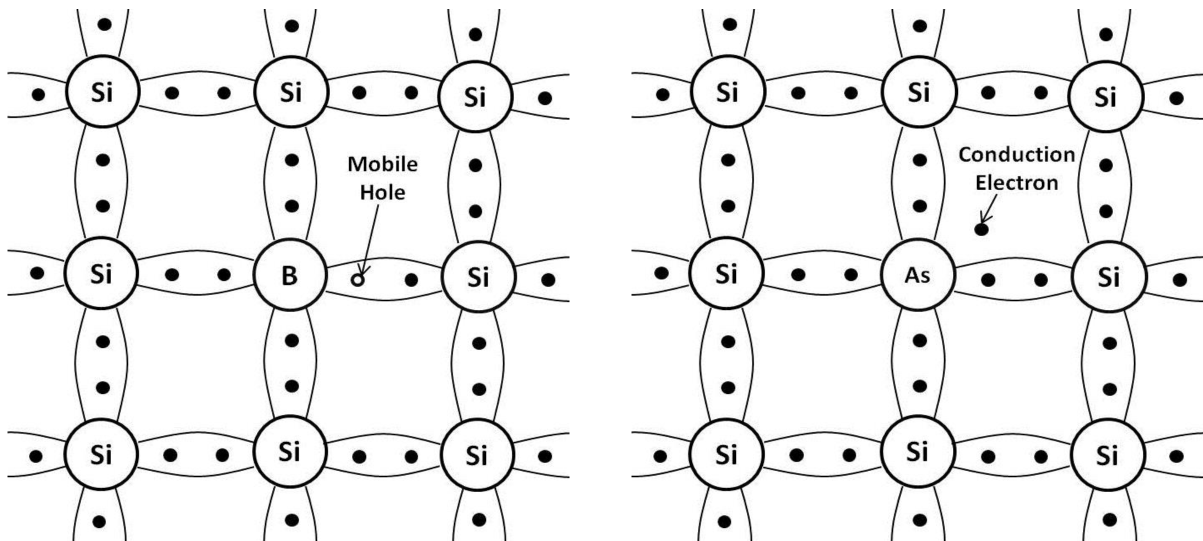

Figure 3.1 Representation of p-type silicon (boron doped) and n-type silicon (phosphorous doped)

As shown in above figure 3.1, the bond model is used to describe that a tetravalent silicon atom can be replaced either by pentavalent atom (group V) or a trivalent atom (group III). When arsenic (group V element) atom with five valence electrons is added to silicon, it forms covalent bonds with its four neighboring silicon atoms and the fifth valence electron due to relatively small binding energy to its arsenic host atom becomes a conduction electron at moderate temperature. This arsenic atom is called a donor and a donor doped material is denoted as n-type semiconductor. Such a doped material has a defined excessive electron (majority carriers) in the

conduction band, while the holes in the valence band, being few in number, are the minority carriers. In a similar way, figure 3.1 demonstrates the behavior of boron doped silicon (p-type silicon). Doped boron atom replaces a silicon atom, thus creating hole carrier in the valence band, therefore boron is referred as an acceptor impurity and form a p-type semiconductor. These dopant impurities used to control the conductivity of semiconductor material usually have very small ionization energies.

3.4 Ion Implantation Technology

Ion Implantation is a materials engineering process by which a focused beam of ions of a material are accelerated by electric fields and separated by magnetic fields and directed towards a target solid. This process is used to change the electrical and chemical properties of the targeted material. These ionized atoms have enough kinetic energy to penetrate into the material upon impact which causes a structural change, i.e. crystal structure of the target wafer can be either damaged or destroyed by these energetic ionized atoms. The basic feature of an ion implanter was invented by Shockley in 1957. The wafers are moved in and out of the vacuum by automated handling systems and processed one at a time or in batches.

The ion source of implanter must be capable of producing stable beams of the common dopants belong to III and V group in periodic table such as boron, phosphorus, arsenic, antimony, and indium.

3.4.1 Process Parameters for Ion Implantation

The ion implantation process is determined by following process parameters [65]:

(i) Dopant species

(ii) Ion beam energy and implantation dose

(iii) Tilt and twist angles

The easiest semiconductor device is the pn-junction diode (transistor) which can be simply fabricated by ion implantation.

Ion implantation is process in which each ion follows an individual trajectory determined by their interactions with the target material atoms. The final position of an implanted ion would be just where it has lost all of its kinetic energy. The average depth of the dopant distribution is referred as the mean projected range (R_p) and the point where the donor and acceptor concentrations are equal is called the junction depth (X_j). Both of these parameters are shown in figure 4.4 of chapter 4.

(i) Dopant Species

Numerous dopant species are used for ion implantation applications as per needs. The Table summarizes some properties of the most important dopants (usually III and V group species) for MOSFET technology.

Table 3.1 Parameters of common doping in silicon [65]

Species	Type	Atomic number	Mass (amu)
Boron	P	5	11.009
Phosphorous	N	15	30.974
Arsenic	N	33	74.922
Germanium	-	32	71.922
Antimony	N	51	120.904

As listed in the table 3.1, boron is the common p-type dopant, whereas phosphorous, arsenic, and some time antimony are used for n-type doping. If different ions with the same energy are implanted, the heavier ions stop at shallower junction relative to the lighter ions due to the atomic mass. The boron atom (a very light atom) would have the broadest distribution and the largest projected range R_p, as a deeper penetration gives rise for more random collision with the target material atoms.

(ii) Ion Energy and Dose

The amount of implanted ions is expressed by the dose (ions/cm^2) and penetration depth of these ions is mainly controlled by ion energy. This energy spans from 100 eV to 3 MeV, and the dose ranges from 10^{11} to 10^{16} ions/cm^2. Typically energies with few keV at high dose are used to achieve ultra-shallow junctions, whereas medium range energies are required to attain poly doping or halo implant. Higher energies with low dose are used for the applications such as retrograde wells. Lower mass atoms are typical implanted at lower energies than heavier species as per doping applications. The dose (ions/cm^2) depends on device design requirements, however independent of the dopant species. The process parameters dose and implantation energy can be controlled quite accurately through electrical measurements. Figure 3.2 shows the experimentally measured mean projected range R_p of the few dopant species as a function of the implantation energy [66, 67]. From figure 3.2 it can be interpreted easily that lower mass species have the larger projected range as described earlier. Thus, boron has the largest projected range of all the dopants, while antimony has the short projected range due to a large difference in masses.

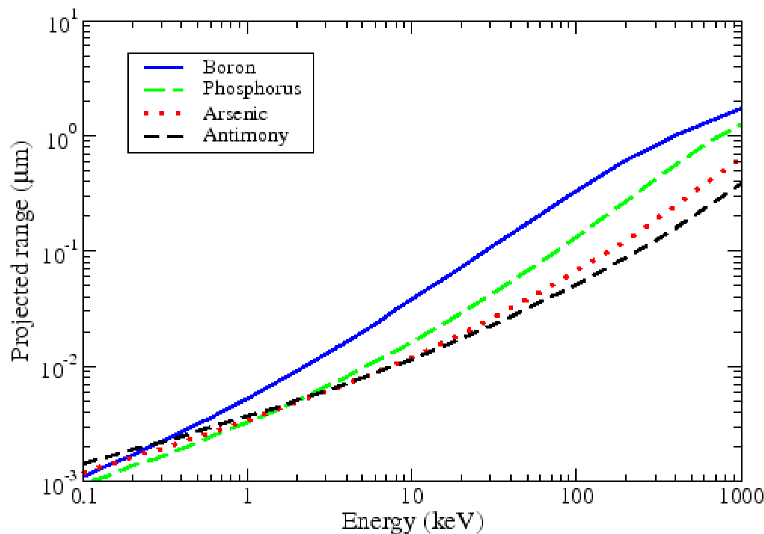

Figure 3.2 Projected range (R_p) for some common dopants in silicon [65].

The total dose Q is the area under the dopant concentration profile $C(z)$ from the wafer surface to at least the junction depth X_j, is given by

$$Q = \int_0^{\infty} C(z)dz \approx \int_0^{Xj} C(z)dz$$

The maximum reasonable dose around 10^{16} cm^{-2} aimed at the formation of highly conductive regions and is confirmed by the solid solubility of the dopant species in the target material. For dopant concentrations greater than the solid solubility, the excessive dopants would precipitate and form immobile clusters during the Rapid thermal Annealing (RTA) process and therefore cannot be activated.

(iii) Tilt and Twist Angle

The ion beam direction with respect to the wafer crystal orientation is defined by the tilt and twist angle, as shown in figure 3.3. The angle between the ion beam and the normal to

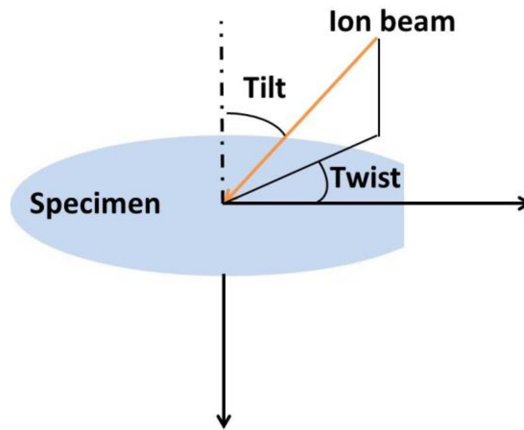

Figure 3.3 Definition of tilt and twist angle for the ion beam.

wafer surface is defined as tilt angle. Wafer rotation or twist is described as the angle between the plane containing the beam and the wafer normal, and the plane perpendicular to the primary flat of the wafer containing the wafer normal.

Chapter 4: Electrochemical Anodic Oxidation

4.1 Silicon Dioxide (SiO_2) thin films

Silicon dioxide (SiO_2) insulating thin films are most widely used in the production of silicon-based semiconductor devices such as integrated circuits (ICs), microelectrochemical systems (MEMS), masking against implantation of dopants in the silicon, gate components in metal oxide semiconductor field effect transistors (MOSFET) [68, 69] etc. Silicon dioxide (SiO_2) is preferred over other insulating films (dielectric films) due to its ease of fabrication, exceptional insulating properties, selective etching and high quality Si-SiO_2 interface. Physical vapour deposition (PVD) and chemical vapour deposition (CVD) are common techniques to grow high quality SiO_2 oxide thin film thermally and are widely employed [70]. However, high processing temperature (~1100^0C) causes redistribution of dopants in silicon substrate during oxidation and develops stress at Si-SiO_2 interface during oxide growth which leads to twist or bend silicon wafer and silicon oxide [71-73]. Several new ways have been developed to reduce the process temperature. Plasma enhanced chemical vapour deposition (PECVD) [74], atmospheric pressure chemical vapour deposition (APCVD) [75], sputtering [76], liquid phase deposition [77], wet anodic oxidation [78-79] are few low temperature thin film deposition techniques, however every process has its own pros and cons. Among these low temperature methods, anodic oxidation is one of the promising ways to grow thin films at room temperature or even below it [80]. Several research groups have studied anodically grown oxide thin films for dielectric elements in MOSFET devices [81, 82]. This oxidation process has a number of advantages over other methods i.e. low cost, the oxide thin film may be doped with electrolyte

ions, simple experimental setup, and a room temperature process which does not involve any toxic gases and minimizes the dopants redistribution.

4.2 Experimental setup

In the past, organic solvents such as N-methyl –acetamide (NMA), tetrahydrofurfuryl alcohol (THFA) and methanol containing an inorganic salt have used as an electrolyte for electrochemical anodic oxidation [80]. In present work, 90 % ethylene glycol (EG), 10 % deionised water (DI water) and a salt of 0.05M concentration potassium nitrate (KNO_3) is used an electrolyte [83]. Here, we investigate thin films grown using anodic oxidation of ion implanted silicon under potentiostatic conditions, i.e. when the applied voltage between the silicon anode and a platinum cathode is kept constant and the current through the anodic circuit changes with time during the process.

The electrolyte cell consists of 100 ml of solution in a beaker of 250 ml above which two alligator clips are suspended as showed in figure 4.1. One clip leads from positive output of a constant voltage source is attached to the silicon (anode), the other is connected to platinum mesh (cathode). Both electrodes are inserted in the electrolyte. The anodic oxidation is performed under constant voltage conditions, i.e. potentiostatistically, at room temperature (22^0C). As evolved gas bubbles stick to the sample causing non uniform oxide growth, magnetic stirrer is used to agitate solution. The current variation with time is also monitored. For each specimen oxidation, a fresh electrolyte is prepared to avoid contamination of the solution by uptake of water or by decomposition products.

The chemical reactions [83] for this electrolyte solution are,

$$C_2H_4(OH)_2 \leftrightarrow 2HCHO + 2H^+ + 2e^-$$

$$Si + 2H_2O \rightarrow SiO_2 + 2e^- + 2H^+$$

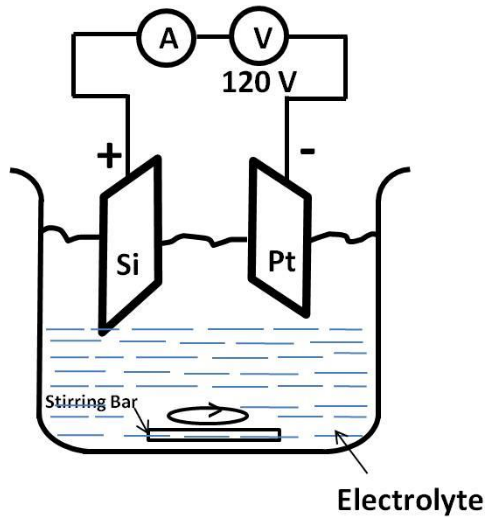

Figure 4.1 Electrochemical anodic oxidation set up

4.3 Study of SiO_2 growth electrochemically and influences of other parameters

Figure 4.2 shows the silicon oxide thickness as a function of the applied voltage for a fixed anodization time 10 minutes.

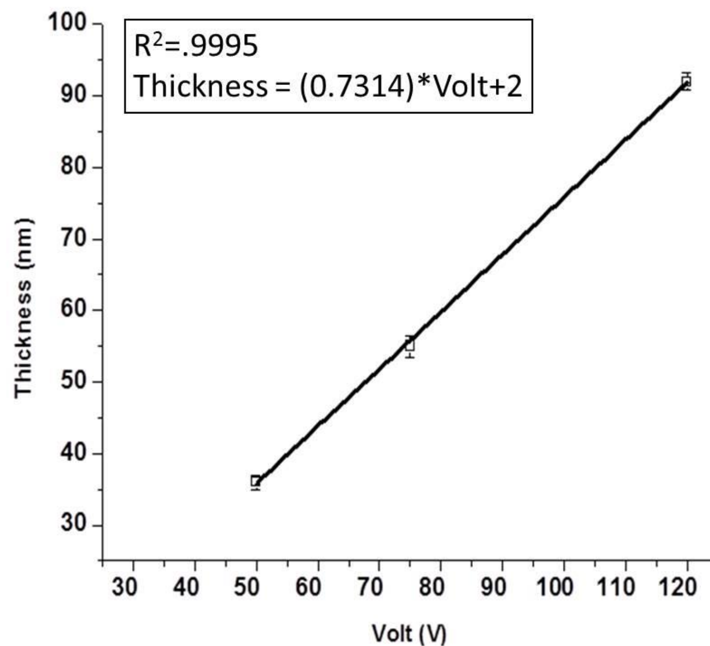

Figure 4.2 Silicon oxide thin film growth study with voltage.

The change of oxide film thickness with applied voltage can be expressed by the following relationship

$$d_{ox}^{exp} = d_{ox}^{0} + mV \tag{4.1}$$

Where, d_{ox}^{exp} is the experimental oxide thickness, d_{ox}^{0} is the thickness of native (air-formed) oxide, m is a constant and V is the applied voltage. From the figure 4.2, we yield

$d_{ox}^{0} = 2.0$ nm and m $= \frac{0.7314}{\mathrm{V}}$

The theoretical value of oxide thickness can be calculated by

$$d_{ox}^{theor} = \frac{Q_{pass}M}{zF\rho} \tag{4.2}$$

Where, Q_{pass} is area under current-time plot (120V and 10 minutes are considered), i.e. $Q_{pass} = current * time$ for anodization process and the value is 3 C/cm^2

M is the molecular weight of silicon oxide = 44 g

z is the number of electrons transported during anodization = 4

F is the Faraday constant = 96500 C and

ρ is density of silicon oxide = 2.65 g/cm^3

Inserting the above values in equation 4.2, we calculate theoretical silicon oxide thickness, which comes out be d_{ox}^{theor}= 1300 nm

From figure 4.2, we get the experimental measured oxide thickness

d_{ox}^{exp}= 90 nm

With the help of equation 4.1 and 4.2, we can calculate growth efficiency

$$n = \frac{d_{ox}^{exp}}{d_{ox}^{theor}}$$

Combining all the above equations, we obtain the growth efficiency of this oxidation process, which is

$$n = 6\ \%$$

Which means that only 6 % of the charge passed supports the silicon oxide growth whereas the remaining 94 % of the charge is consumed for the creation of non-growth current, i.e. mainly electronic and dissolution currents. This calculation is done from the reference [80].

In this work, we also study the impact of time on the growth of oxide at two different voltages (100 V and 120 V). It can be easily seen that as thickness of oxide increases with the time, however for longer period it does not increase so fast.

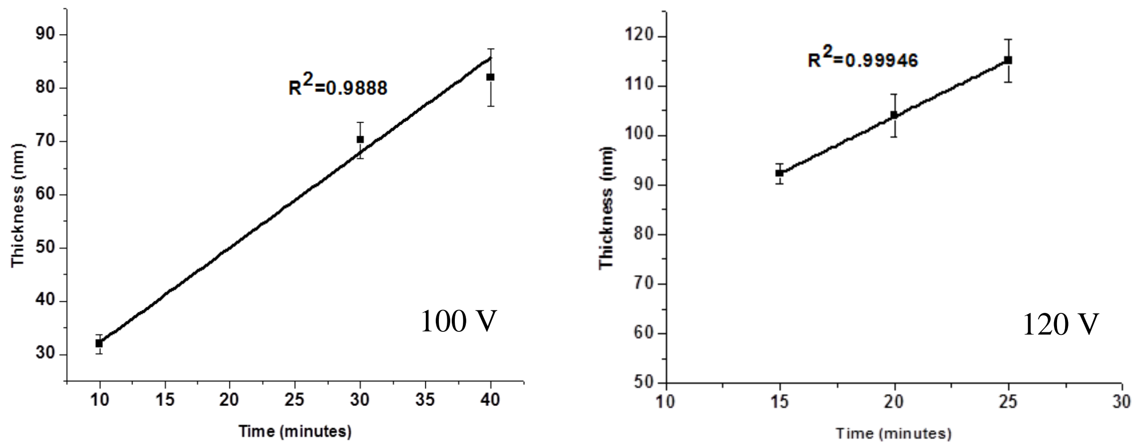

Figure 4.3 Study of silicon oxide growth with time at 100 V and 120 V.

4.4 Sample preparation

The doping profile mapping is demonstrated in a regular silicon wafer (CZ, 475-575 µm, boron –doped, (100), 10-25 Ω-cm) and one face mechano-chemically polished. A thin film of ~17 nm dry oxide is grown on wafer surface using a Bruce furnace and the thickness is confirmed through Nanometrics Spectrophotometer. A Varian 350D ion implanter is used to implant phosphorus ions with a dosage of $5 * 10^{15} \mathrm{atoms/cm^2}$ into the sacrificial oxide layer at

60 keV energy. Subsequently rapid thermal annealing (RTA) is done to activate the dopant to go in interstitial sites. Hydrofluoric acid (HF) is used to remove the top dry oxide layer. The resulting doping profile is measured from SIMS (Secondary Mass Ion Mass Spectrometry), Qspec Inc., as depicted in the figure 4.4 with an uncertainty of $\pm 5\%$ in measurement.

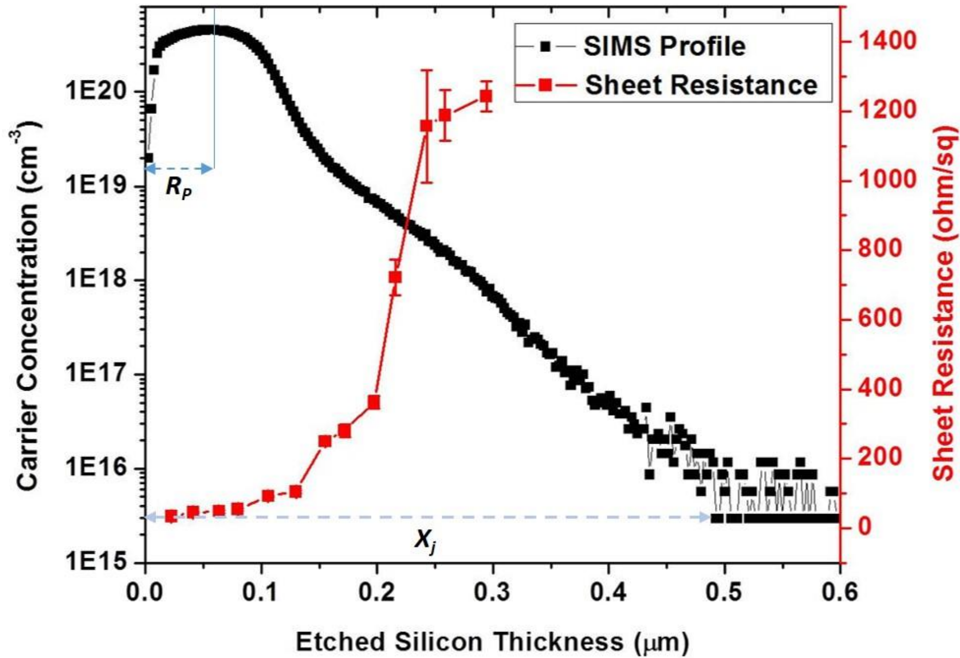

Figure 4.4 SIMS profile of the sample and sheet resistance measurements with respect to etched silicon.

The ion-implanted silicon wafer is diced in approximately 16 pieces. In our experiment, we supply the constant voltage 120V for 5-10 minutes to grow approximately 50-90 nm of silicon oxide thin film. To protect the backside from oxidation, we wrap another silicon sample, with approx. 1.2 μm thick silicon dioxide during entire process. Thirteen samples are prepared using anodic oxidation process. These samples are 20, 40, 60, 80, 100, 130, 160, 170, 200, 220, 240, 260, and 320 (in nanometers) in terms of etched silicon thickness. The thickness of anodic silicon oxides are carried out using ellipsometer (Rudolp IV ellipsometer). The successful oxidation is confirmed by measuring sheet resistance change in samples after removal of oxide

thin film using buffer oxide etch (BOE consists of ammonium fluoride & HF, 10:1). The sheet resistance is measured using four point probes method (CDRES Map) and shown in figure 4.4. The sheet resistance starts increasing when we remove the carriers in the ion implanted sample as depicted in figure 4.4.

Chapter 5: Results

5.1 THz measurements in time domain

The photoconductive system at RIT has the frequency bandwidth limited around 1.2 THz and can be potentially extended up to 8 THz using plasma system. The THz measurements and data analysis are done on all the samples fabricated (using anodic oxidation) to clearly observe the THz radiation change with carrier concentration. All the samples are characterized for the doping profile demonstration. The peak concentration and junction depth is $\sim 4\times10^{20}$ cm^{-3} and 450 nm respectively in as-implanted sample here at RIT SMFL (Semiconductor and Microsystems Fabrication Laboratory). The implantation energy 60keV drives phosphorus atoms to a deeper location, origins the bump in profile in heavily doped region during the annealing process. After etching 320 nm Silicon, the peak concentration reduces to $\sim 3\times10^{17}$ cm^{-3}. The SIMS measures the lower detection limit at 3×10^{15} cm^{-3}; whereas sheet resistance measurement estimates substrate concentration to be approximately 1.2×10^{15} cm^{-3} as shown in figure 4.4 in previous chapter. We define $\sim 1.2\times10^{15} cm^{-3}$ as the substrate concentration in our modeling process.

Figure 5.1 shows the THz pulse change in the time domain for few samples, which demonstrate again the profile recognition ability reported in previous work by C. J. Yen et al. [84]. As we begin etching heavily doped regions, the amplitude (mV) of THz radiation increases as a function of removal oxidation thickness. The black curve is the reference air scan in this case and gives the maximum THz transmission which is approximately 1 mV amplitude. The silicon sample's, 1st internal reflection peak has a bigger shape distortion and smaller amplitude change, which results from the $\times 3$ traveling patch inside the sample. The peak amplitude increases with the removal of more doped silicon and the peak location starts shifting to left as

we start etching the doped regions. Time domain plots help us to recognize the doping concentration change and plentiful information in the frequency domain to map the accurate profile.

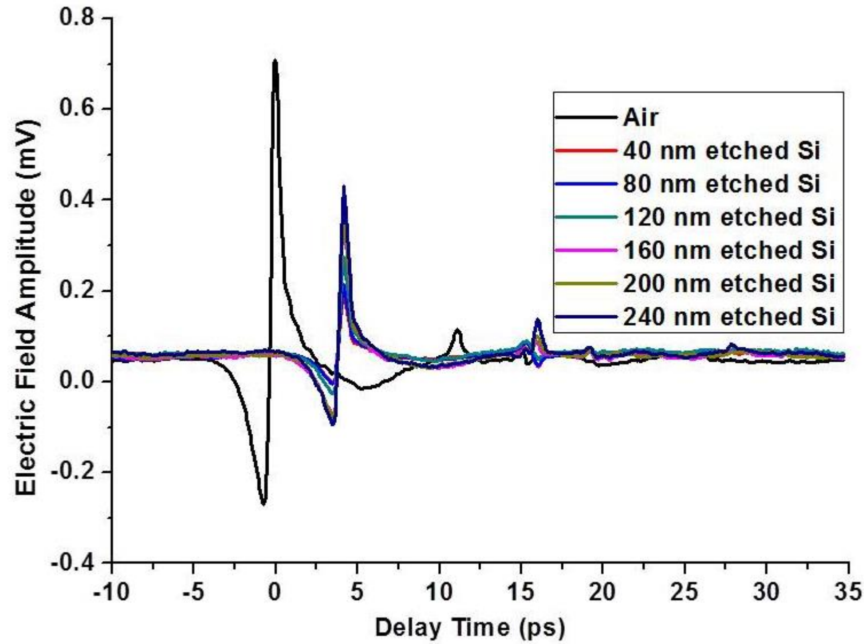

Figure 5.1 Time domain measurements of silicon samples.

5.2 Demonstration of Reverse mapping of doping profile

The earlier published work by Chih Yu et al. indicates that the doping profile has unique dispersion (different phase shift between different frequencies) and also unique patterns of internal reflection at different frequencies [84]. These results have unique transmission spectrum and could be considered similar to fingerprint. Considering all these factors, the power transmission ratios in the frequency domain delivers a sensitive indicator to dopants concentration. This encourages us to predict doping profile using frequency domain spectra. Reverse mapping is considered as an example to demonstrate profile construction. The detailed

process of doping profile prediction is illustrated in Figure 5.2. In our experiments, air scan is defined as the reference for the calculation of power transmission ratio.

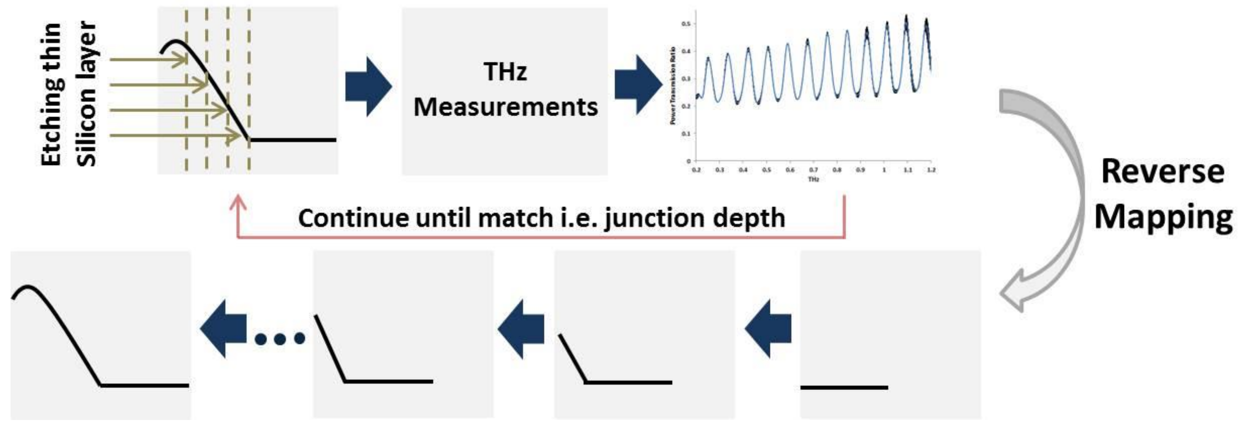

Figure 5.2 Demonstration of reverse mapping via destructive way

Considering samples with known doping profiles, the anodic oxidation technique is used to remove fixed thickness of silicon in each cycle. It can be applied either on the same spot of the sample each time to etch fixed thickness or couple of pieces (samples) diced from the wafer to target particular thickness independently. A better thickness control and high THz measurement accuracy are expected using the 2nd option, which is implemented here in this theses work. The THz measurements usually consist of air, Si substrate and ion implanted Si sample. The air and ion implanted sample (with different etched layers of ion implanted silicon wafer) scans are used to construct the doping profile in each cycle and the silicon substrate scan is used as a reference to detect the junction depth. The profile junction depth can be determined when both the ion implanted sample and silicon substrate THz spectra are almost identical. The residual doping profile is considered as the substrate carrier concentration (intrinsic carriers in silicon). Based on the empirical refractive index information from C. Y. Jen et al. (manuscript submitted), the residual profile induced THz absorption should be negligible. The etched silicon thickness is typically calculated from the measured SiO_2 thickness multiplied by a fixed ratio of 0.46. Precise

thickness of etched silicon is essential to determine the profile concentration. The determination of other key factors, substrate concentration and thickness, can be found in another previous work [85]. The profile construction process initiates from the last etched sample (where the junction depth is) and concludes with the as-implanted sample. That's why we call it "*Reverse Mapping*" in our research. In the backward prediction process, the profile predicted in the "(n+1) th" cycle sample is used as the basis to estimate the "n th" cycle segment concentration. The segment concentration is determined by achieving a negligible (minimum) difference in power ratio between the THz measurements and the predicted power ratio from the transfer matrix (chapter 2, section 2.4). The derived equation (ML-Two Peaks equation, chapter 2, section 2.4) is applied to estimate the complex transmission accurately from the first two THz peaks through the empirical refractive index (C. Y. Jen et al., manuscript submitted). In this demonstration, the substrate concentration is considered $\sim 1.26\times10^{15}$ cm^{-3}, the substrate thickness is 523μm and the modeling region is 500 nm (the profile junction depth from SIMS). 25 segments with 20nm section width are used in the modeling process. Figure 5.3 shows both experimental and theoretical power ratios for all the samples. The difference in is negligible for both experimental and modelling process spectra. Reiterating the same procedure, the doping profile is constructed step by step as shown in figure 5.3.

5.3 Experimental and theoretical results

Here we discuss both the experimental and theoretical power transmission ratio for all the fabricated samples. The profile is predicted using the SIMS profile.

320 nm etched Silicon

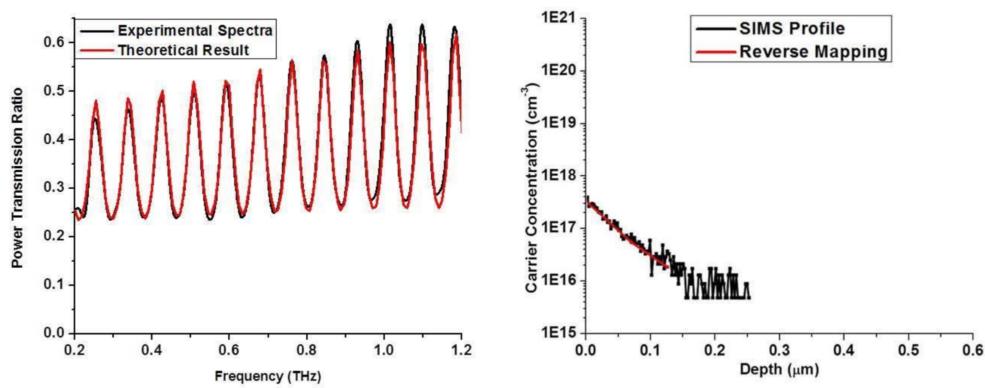

260 nm etched Silicon

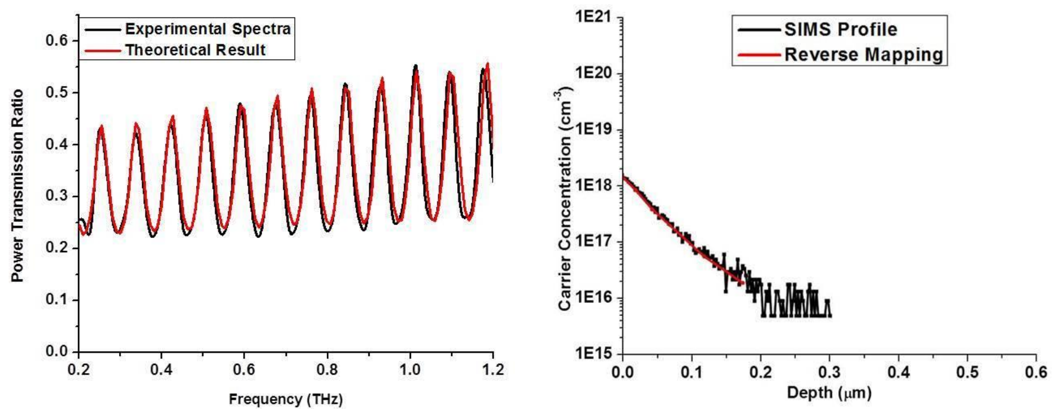

240 nm etched Silicon

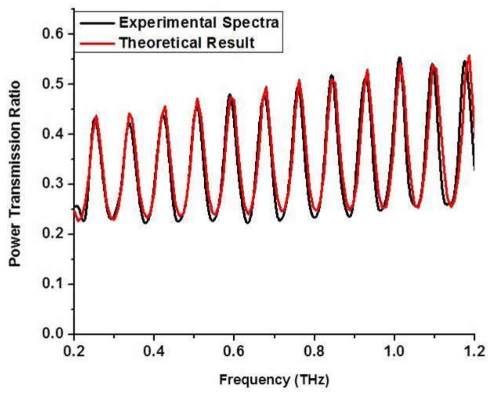

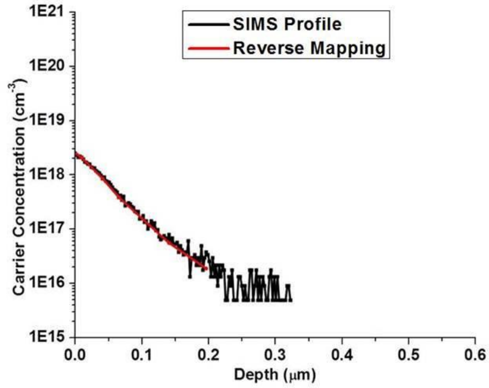

220 nm etched Silicon

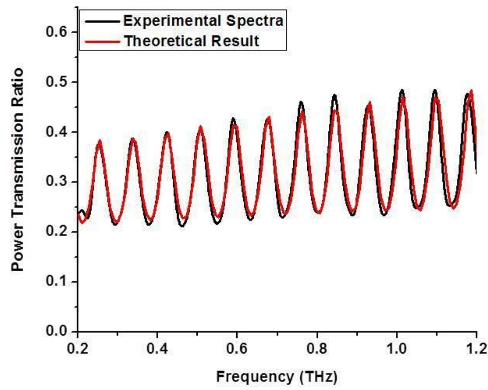

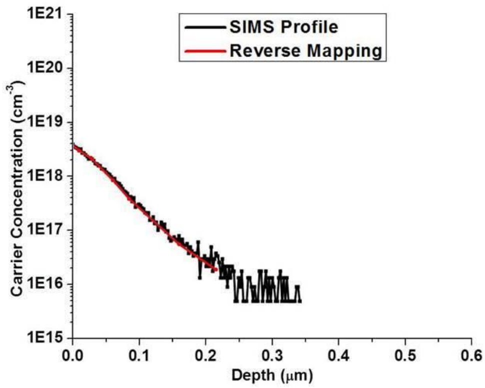

200 nm etched Silicon

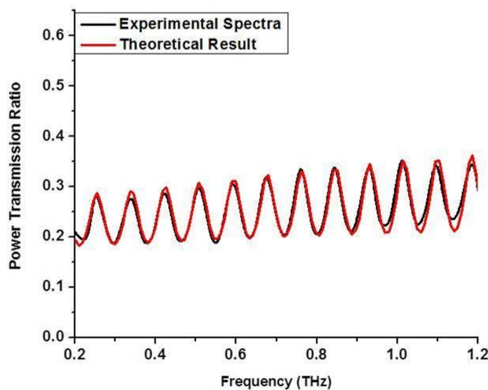

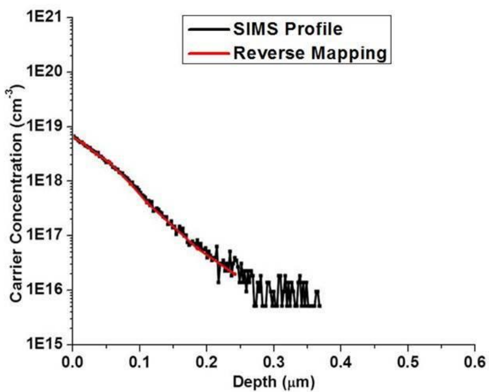

170 nm etched Silicon

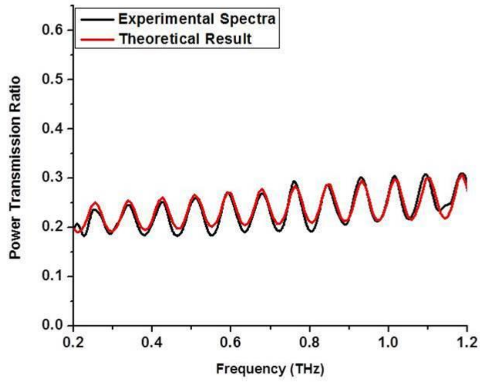

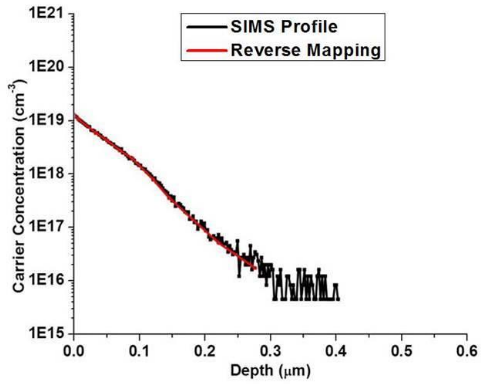

160 nm etched Silicon

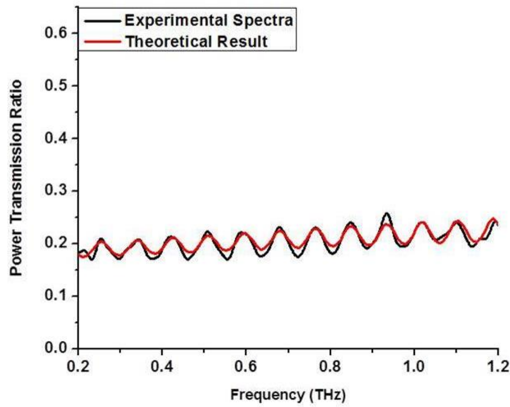

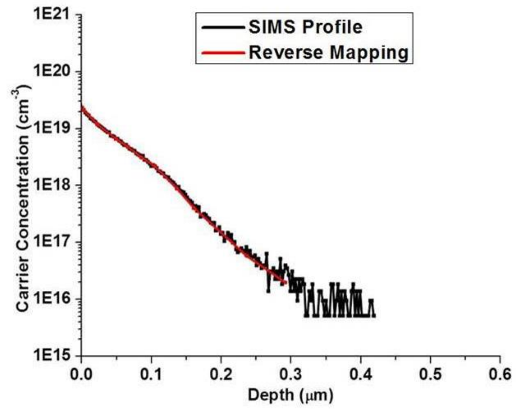

130 nm etched Silicon

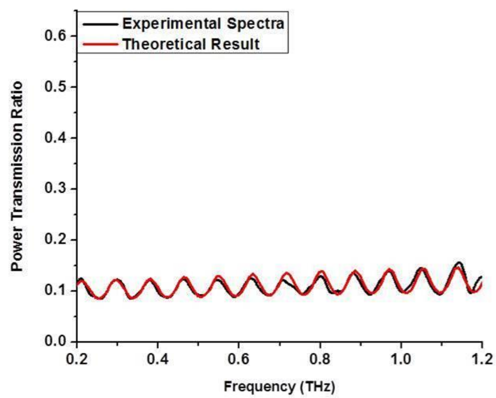

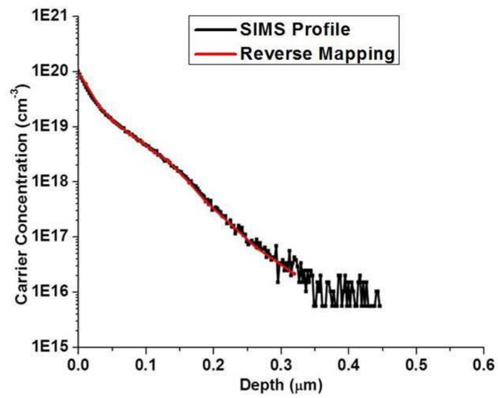

100 nm etched Silicon

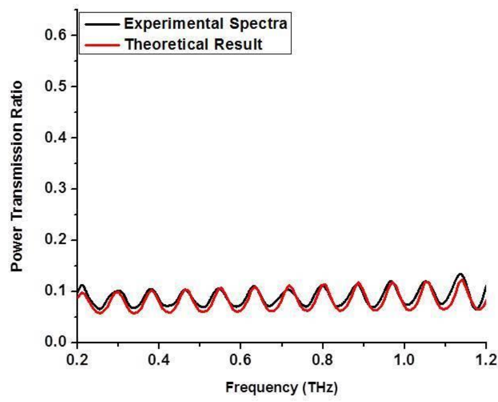

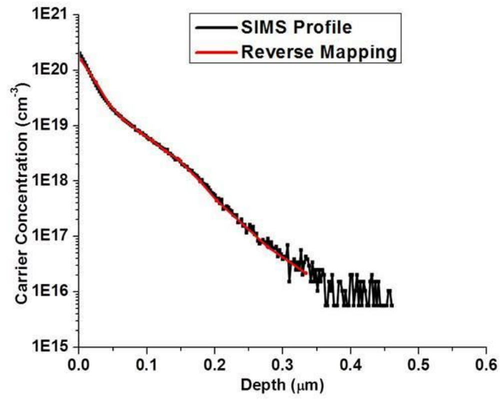

80 nm etched Silicon

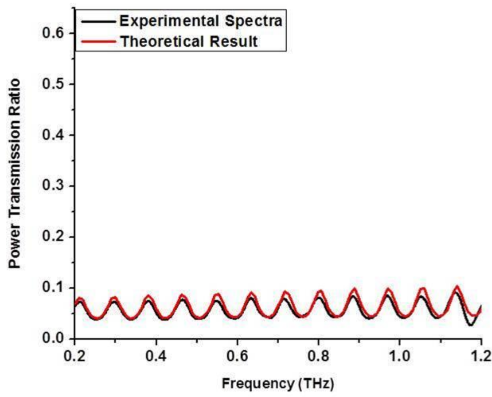

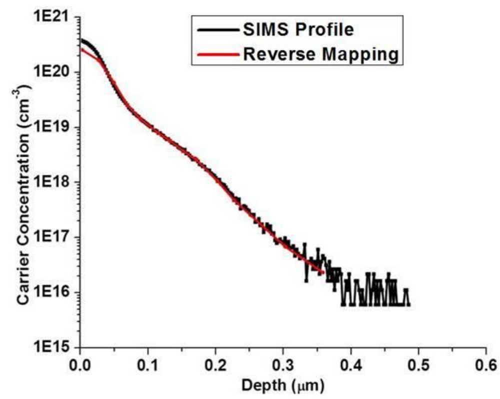

60 nm etched Silicon

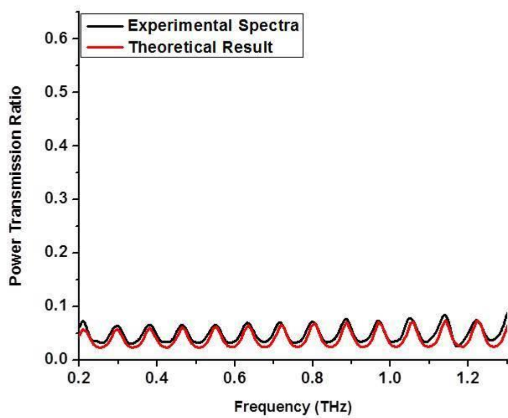

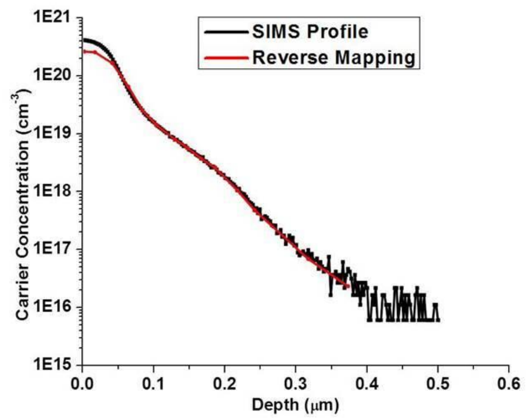

40 nm etched Silicon

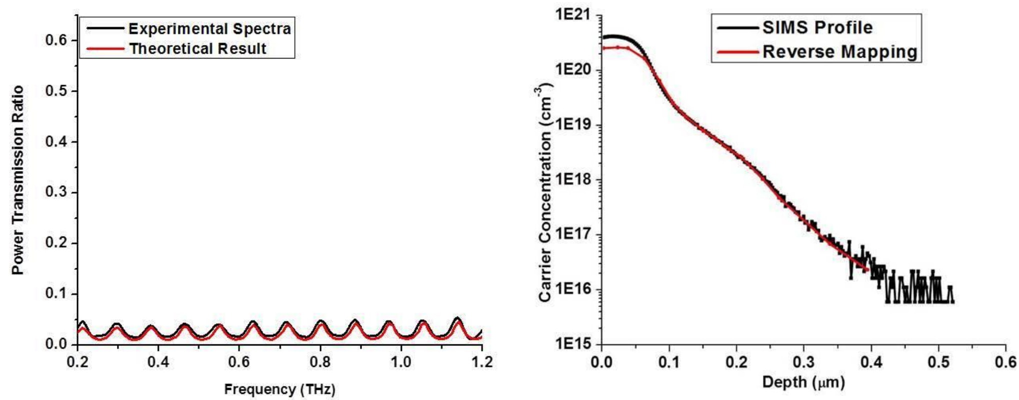

20 nm etched Silicon

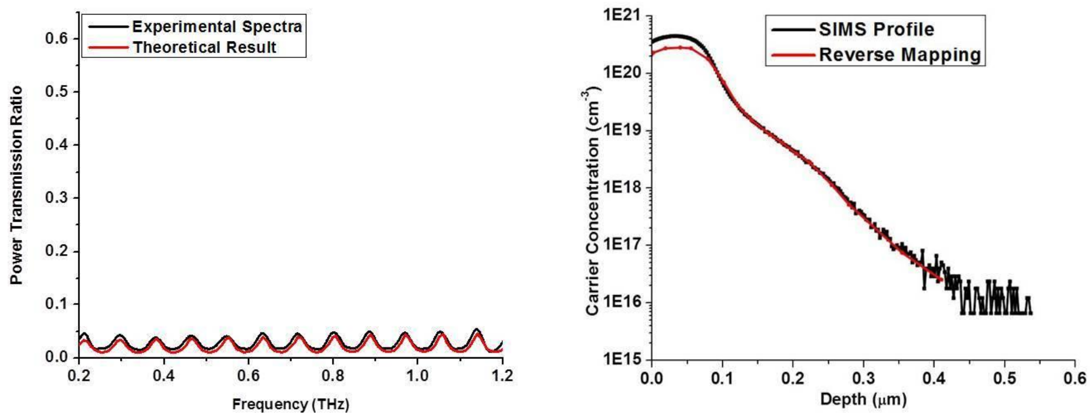

Figure 5.3 Both experimental and predicted results (spectra and reverse doping profile).

5.4 Doping profile using sheet resistance (Irvin's curve)

For simple doping profiles, following Gaussian or complementary error function (erfc) distributions, sheet resistances (R_s) can be readily used to understand carrier concentrations using Irvin's curves [86]. In chapter 4, figure 4.4, we observe that sheet resistance (R_s) increases as the carrier concentration decreases. What should be the best possible result if we use sheet resistance combined with the etched Si layer to predict doping profile? In the practice, the n-type Gaussian Irvine's curve with substrate concentration of 10^{15} cm^{-3} is selected to determine peak

concentrations of all cycle etched samples through their R_s measurements. Multiplying R_s with corresponding junction depth gives us the R_sX_j value to estimate the surface carrier concentration. Lastly, plotting these carrier concentrations from the Irvin's curve to junction depth yields the approximated doping profile, shown in Figure 5.4.

5.5 Benchmark and comparison

Figure 5.4, shows the doping profiles measured using SIMS, sheet resistance and THz time domain spectroscopy. Doping profile measured using sheet resistance provides a rough idea where as SIMS and our THz-TDS technique matches quite closely except in heavily doped regions. This is explained by chemical profile versus electrical profile. SIMS measures the concentration of all the phosphorous atoms (both interstitial and substitutional atoms) whereas THz measures only electrically active i.e. substituitonal phosphorous atoms.

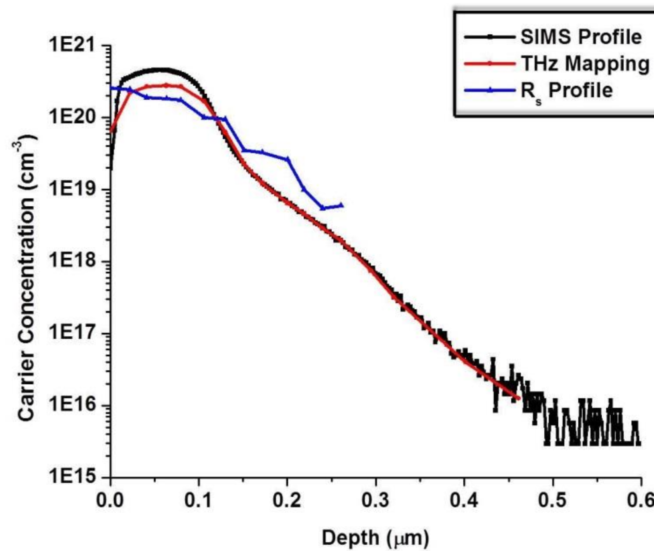

Figure 5.4 Doping profile presentation using SIMS, sheet resistance and our method (THz-TDS).

Chapter 6: Conclusion

Here we demonstrate, the transmission mode terahertz-Time Domain Spectroscopy (THz-TDS) combined with the electrochemical anodic oxidation (destructive) technique to study electrically active phosphorus dopants to map doping profile in non-contact way. In this work, the anodic oxidation is carried out to achieve a controllable SiO_2 thin film (can be attained up to 1 nm) to remove précised silicon layer. Predicted doping profile is benchmarked with the standard technique SIMS (Secondary Ion Mass Spectrometry) and doping profile using sheet resistance with Irvine's curve. It is obvious from the figure 5.4 that SIMS measurement is in good agreement with doping profile prediction using the new concept, but profile using sheet resistance is somewhat gives us a rough idea. Although both techniques have some limitations. Relative to the SIMS profile, the predicted profile carrier concentration is lighter in heavily doped regions but quite consistent in moderate and lightly doped regions. This phenomenon is pretty reasonable and can be explained by considering the difference between a chemical doping profile and an electrical doping profile. Many previous published papers indicate that inactive dopants are typically created in a diffusion process or an ion implanted process with a highly inserted dosage and the induced profile difference has been studied using both ECV and SIMS methods [2, 87-88]. The plateau profile is frequently observed via ECV in heavily doped regions. The profile difference in figure 5.4 identifies the same behavior since THz-TDS measures the free carriers to predict electrical doping profile, similar to ECV.

As expected, the predicted doping profile from Irvine's curve doesn't seem to be in good agreement with other techniques. Doping profile via sheet resistance is typically applicable if junctions are reasonably deep and not easy to deal with profiles with shallow junctions. Furthermore, if the concentration profile is neither in Gaussian nor in complementary error

function form, obtained result will be incorrect, inconclusive and will provide inconsistent profile. Industries mostly deal with shallow junction profiles these days, therefore mapping doping profile using sheet resistance from Irvin's curve would not be a right practice.

Relative to other standard practices, the profile we generate has an advantage over others to reflect reasonably more accurate electrical performance with spectra in THz regions. With the usage of the derived "ML-Two Peaks" equation and empirical refractive index information (C. Y. Jen et al., manuscript submitted), the experimental results indicate that estimated power transmission ratios match quite well with the THz spectra measurements for almost all samples. THz measurements are reiterated to see the reproducibility of spectra in two different time frames and found that these are quite consistent. Electrochemical oxidation is considered to grow and control silicon oxide thickness in this work; however from the industry applications perspective, other methods can be considered as alternative options to achieve same or even better thickness resolution. Reverse mapping is proposed to demonstrate the doping profile construction. The reverse way to map doping profile uses simple and straight forward concept to construct it in a reverse sequence. The outcome points a significant discrepancy in heavily doped regions, which can be interpreted as inactive atom dopants in this region as described earlier. Furthermore, the profile prediction from Irvine's curve doesn't come close to any of the described method for the shallow junctions. In this research, essential information from (C. Y. Jen et al., manuscript submitted) is implemented to predict the doping profile in a destructive way using THz-TDS. The relative stand-alone system can be designed to measure the doping profile remotely like other destructive techniques. The transmission mode schematic is only applicable for samples with THz survived after the light penetration. This method can be utilized to study dopants in other semiconducting materials like III-V group. The estimated doping

profile should provide the important message (C. Y. Jen et al., manuscript submitted) to benefit the future device modeling in THz regions in semiconductor and photonics industries.

References

1. Naruse, M., Sekimoto, Y., Suzuki, T., Hibi, Y., Matsuo, H., Uzawa, Y., & Noguchi, T. (2009, September). Design of SIS imaging array for terahertz astronomy. In *Infrared, Millimeter, and Terahertz Waves, 2009. IRMMW-THz 2009. 34th International Conference on* (pp. 1-2). IEEE.
2. Peiner, E., Schlachetzki, A., & Krüger, D. (1995). Doping Profile Analysis in Si by Electrochemical Capacitance-Voltage Measurements. *Journal of the Electrochemical Society*, *142*(2), 576-580.
3. Ashworth, P. C., Pickwell-MacPherson, E., Provenzano, E., Pinder, S. E., Purushotham, A. D., Pepper, M., & Wallace, V. P. (2009). Terahertz pulsed spectroscopy of freshly excised human breast cancer. *Optics express*, *17*(15), 12444-12454.
4. Fitzgerald, A. J., Berry, E., Zinovev, N. N., Walker, G. C., Smith, M. A., & Chamberlain, J. M. (2002). An introduction to medical imaging with coherent terahertz frequency radiation. *Physics in Medicine and biology*, *47*(7), R67.
5. Humphreys, K., Loughran, J. P., Gradziel, M., Lanigan, W., Ward, T., Murphy, J. A., & O'sullivan, C. (2004, September). Medical applications of terahertz imaging: a review of current technology and potential applications in biomedical engineering. In *Engineering in Medicine and Biology Society, 2004. IEMBS'04. 26th Annual International Conference of the IEEE* (Vol. 1, pp. 1302-1305). IEEE.
6. Schirmer, M., Fujio, M., Minami, M., Miura, J., Araki, T., & Yasui, T. (2010). Biomedical applications of a real-time terahertz color scanner. *Biomedical optics express*, *1*(2), 354-366.
7. Luo, J. J., Hou, S. X., Xu, J., & Li, J. J. (2007, September). Study on applications of terahertz technology. In *International Symposium on Photoelectronic Detection and Imaging: Technology and Applications 2007* (pp. 662203-662203). International Society for Optics and Photonics.
8. Kopeika, N. S., Abramovich, A., Yadid-Pecht, O., Yitzhaky, Y., Belenky, A., Lineykin, S., & Rozban, D. (2008, December). Relatively inexpensive terahertz imaging. In *Electrical and Electronics Engineers in Israel, 2008. IEEEI 2008. IEEE 25th Convention of* (pp. 137-141). IEEE.
9. Woodward, R. M. (2005, May). Terahertz technology in global homeland security. In *Defense and Security* (pp. 22-31). International Society for Optics and Photonics.
10. Etayo, D., Iriarte, J. C., Palacios, I., Maestrojuan, I., Teniente, J., Ederra, I., & Gonzalo, R. (2011, September). THz imaging system for industrial quality control. In Microwave Workshop Series on Millimeter Wave Integration Technologies (IMWS), 2011 IEEE MTT-S International (pp. 172-175). IEEE.
11. Rutz, F., Koch, M., Khare, S., Moneke, M., Richter, H., & Ewert, U. (2006). Terahertz quality control of polymeric products. *International Journal of Infrared and Millimeter Waves*, *27*(4), 547-556.

12. Dean, P., Valavanis, A., Scheuring, A., Stockhausen, A., Probst, P., Salih, M., ... & Siegel, M. (2012). Ultra-fast sampling of terahertz pulses from a quantum cascade laser using superconducting antenna-coupled NbN and YBCO detectors. In *2012 37th International Conference on Infrared, Millimeter, and Terahertz Waves (IRMMW-THz)* (pp. 1-2). Institute of Electrical and Electronics Engineers.
13. Eikelboom, J. A., Leguijt, C., Frumau, C. F. A., & Burgers, A. R. (1995). Microwave detection of minority carriers in solar cell silicon wafers. *Solar energy materials and solar cells*, *36*(2), 169-185.
14. Belfer, S., Fainchtain, R., Purinson, Y., & Kedem, O. (2000). Surface characterization by FTIR-ATR spectroscopy of polyethersulfone membranes-unmodified, modified and protein fouled. *Journal of Membrane Science*, *172*(1), 113-124.
15. Jen, C. Y. (2014). Silicon Doping Profile Measurement Using Terahertz Time Domain Spectroscopy.
16. Liu, G. L., Uchida, H., Aikawa, I., Kuroda, S., & Hirashita, N. (1996). Accurate secondary ion mass spectrometry analysis of shallow doping profiles in Si based on the internal standard method. *Journal of Vacuum Science & Technology B*, *14*(1), 324-328.
17. Zelsacher, R., Wood, A. C. G., Bacher, E., Prax, E., Sorschag, K., Krumrey, J., & Baumgartl, J. (2007). A novel SIMS based approach to the characterization of the channel doping profile of a trench MOSFET.*Microelectronics Reliability*, *47*(9), 1585-1589.
18. Mathur, R. (1992). Dopant profile extraction from spreading resistance measurements. *Journal of Vacuum Science & Technology B*, *10*(1), 421-425.
19. Ishida, E., & Felch, S. B. (1996). Study of electrical measurement techniques for ultra-shallow dopant profiling. *Journal of Vacuum Science & Technology B*,*14*(1), 397-403.
20. Wu, H. Z., Ru, G. P., Jin, C. G., Mizuno, B., Jiang, Y. L., Qu, X. P., & Li, B. Z. (2006). ECV Profiling of Ultra-Shallow Junction Formed by Plasma Doping. In*Junction Technology, 2006. IWJT'06. International Workshop on* (pp. 120-122). IEEE.
21. Bentzen, A., & Holt, A. (2005, January). Correspondence between sheet resistance and emitter profile of phosphorus diffused emitters from a spray-on dopant. In *Photovoltaic Specialists Conference, 2005. Conference Record of the Thirty-first IEEE* (pp. 1153-1156). IEEE.
22. Vandervorst, W., & Clarysse, T. (1992). On the determination of dopant/carrier distributions. *Journal of Vacuum Science & Technology B*, *10*(1), 302-315.
23. Tan, L. S., Tan, L. C. P., Leong, M. S., Mazur, R. G., & Ye, C. W. (2002). Characterization of ultrashallow dopant profiles using spreading resistance profiling. *Journal of Vacuum Science & Technology B*, *20*(1), 483-487.
24. Hilibrand, J., & Gold, R. D. (1960). Determination of the impurity distribution in junction diodes from capacitance-voltage measurements. *RCA review*, *21*(2), 245-252.
25. Liu, Z., Zhang, Y., Kok, S. W., Ng, B. P., & Soh, Y. C. (2013). Reflection-based near-field ellipsometry for thin film characterization. *Ultramicroscopy*,*124*, 26-34.

26. Neshat, M., & Armitage, N. P. (2012). Terahertz time-domain spectroscopic ellipsometry: instrumentation and calibration. *Optics express*, *20*(27), 29063-29075.
27. Hofmann, T., Herzinger, C. M., Boosalis, A., Tiwald, T. E., Woollam, J. A., & Schubert, M. (2010). Variable-wavelength frequency-domain terahertz ellipsometry. *Review of Scientific Instruments*, *81*(2), 023101.
28. Lloyd-Hughes, J., & Jeon, T. I. (2012). A review of the terahertz conductivity of bulk and nano-materials. *Journal of Infrared, Millimeter, and Terahertz Waves*,*33*(9), 871-925.
29. Nashima, S., Morikawa, O., Takata, K., & Hangyo, M. (2001). Measurement of optical properties of highly doped silicon by terahertz time domain reflection spectroscopy. *Applied physics letters*, *79*(24), 3923-3925.
30. Pashkin, A., Kempa, M., Němec, H., Kadlec, F., & Kužel, P. (2003). Phase-sensitive time-domain terahertz reflection spectroscopy. *Review of scientific instruments*, *74*(11), 4711-4717.
31. Wu, Q., Hewitt, T. D., & Zhang, X. C. (1996). Two-dimensional electro-optic imaging of THz beams. *Applied Physics Letters*, *69*(8), 1026-1028.
32. Mittleman, D. M., Jacobsen, R. H., & Nuss, M. C. (1996). T-ray imaging. *IEEE Journal of selected topics in quantum electronics*, *2*(3), 679-692.
33. Mittleman, D. M., Hunsche, S., Boivin, L., & Nuss, M. C. (1997). T-ray tomography. *Optics letters*, *22*(12), 904-906.
34. Yasuda, T., Yasui, T., Araki, T., & Abraham, E. (2006). Real-time two-dimensional terahertz tomography of moving objects. *Optics communications*,*267*(1), 128-136.
35. Lee, A. W., Williams, B. S., Kumar, S., Hu, Q., & Reno, J. L. (2006). Real-time imaging using a 4.3-THz quantum cascade laser and a 320/spl times/240 microbolometer focal-plane array. *Photonics Technology Letters, IEEE*, *18*(13), 1415-1417.
36. Kim, S. M., Hatami, F., Harris, J. S., Kurian, A. W., Ford, J., King, D., ... & Harris, G. (2006). Biomedical terahertz imaging with a quantum cascade laser. *Applied physics letters*, *88*(15), 153903-153903.
37. Nagai, N., Sumitomo, M., Imaizumi, M., & Fukasawa, R. (2006). Characterization of electron-or proton-irradiated Si space solar cells by THz spectroscopy. *Semiconductor science and technology*, *21*(2), 201.
38. Nagai, N., Imai, T., Fukasawa, R., Kato, K., & Yamauchi, K. (2004). Analysis of the intermolecular interaction of nanocomposites by THz spectroscopy.*Applied physics letters*, *85*(18), 4010-4012.
39. Misra, M., Kotani, K., Kawayama, I., Murakami, H., & Tonouchi, M. (2005). Observation of TO 1 soft mode in SrTiO 3 films by terahertz time domain spectroscopy. *Applied Physics Letters*, *87*(18), 182909-182909.
40. Mittleman, D. M., Cunningham, J., Nuss, M. C., & Geva, M. (1997). Noncontact semiconductor wafer characterization with the terahertz Hall effect.*Applied Physics Letters*, *71*(1), 16-18.
41. Jen, C. Y., & Richter, C. (2014). Sample Thickness Measurement with THz-TDS: Resolution and Implications. *Journal of Infrared, Millimeter, and Terahertz Waves*, *35*(10), 840-859.

42. Kawase, K., Ogawa, Y., Watanabe, Y., & Inoue, H. (2003). Non-destructive terahertz imaging of illicit drugs using spectral fingerprints. *Optics express*,*11*(20), 2549-2554.
43. Huber, R., Tauser, F., Brodschelm, A., Bichler, M., Abstreiter, G., & Leitenstorfer, A. (2001). How many-particle interactions develop after ultrafast excitation of an electron–hole plasma. *Nature*, *414*(6861), 286-289.
44. Auston, D. H. (1975). Picosecond optoelectronic switching and gating in silicon.*Applied Physics Letters*, *26*(3), 101-103.
45. Dai, J., Liu, J., & Zhang, X. C. (2011). Terahertz wave air photonics: terahertz wave generation and detection with laser-induced gas plasma. *Selected Topics in Quantum Electronics, IEEE Journal of*, *17*(1), 183-190.
46. Schmuttenmaer, C. A. (2004). Exploring dynamics in the far-infrared with terahertz spectroscopy. *Chemical reviews*, *104*(4), 1759-1780.
47. Tonouchi, M. (2007). Cutting-edge terahertz technology. *Nature photonics*, *1*(2), 97-105.
48. Leitenstorfer, A., Hunsche, S., Shah, J., Nuss, M. C., & Knox, W. H. (1999). Femtosecond charge transport in polar semiconductors. *Physical review letters*, *82*(25), 5140.
49. Leitenstorfer, A., Hunsche, S., Shah, J., Nuss, M. C., & Knox, W. H. (2000). Femtosecond high-field transport in compound semiconductors. *Physical Review B*, *61*(24), 16642.
50. Darrow, J. T., Zhang, X. C., Auston, D. H., & Morse, J. D. (1992). Saturation properties of large-aperture photoconducting antennas. *Quantum Electronics, IEEE Journal of*, *28*(6), 1607-1616.
51. Bass, M., Franken, P. A., Ward, J. F., & Weinreich, G. (1962). Optical rectification. *Physical Review Letters*, *9*(11), 446.
52. Yang, K. H., Richards, P. L., & Shen, Y. R. (1971). Generation of Far-Infrared Radiation by Picosecond Light Pulses in LiNbO3. *Applied Physics Letters*, *19*(9), 320-323.
53. Bonvalet, A., Joffre, M., Martin, J. L., & Migus, A. (1995). Generation of ultrabroadband femtosecond pulses in the mid-infrared by optical rectification of 15 fs light pulses at 100 MHz repetition rate. *Applied Physics Letters*, *67*(20), 2907-2909.
54. Ferguson, B., & Zhang, X. C. (2002). Materials for terahertz science and technology. *Nature materials*, *1*(1), 26-33.
55. Kübler, C., Huber, R., & Leitenstorfer, A. (2005). Ultrabroadband terahertz pulses: generation and field-resolved detection. *Semiconductor science and technology*, *20*(7), S128.
56. Miller, A. J., Luukanen, A., & Grossman, E. N. (2004, September). Micromachined antenna-coupled uncooled microbolometers for terahertz imaging arrays. In *Defense and Security* (pp. 18-24). International Society for Optics and Photonics.
57. Yasui, T., Nishimura, A., Suzuki, T., Nakayama, K., & Okajima, S. (2006). Detection system operating at up to 7 THz using quasioptics and Schottky barrier diodes. *Review of scientific instruments*, *77*(6), 066102-066102.
58. Ariyoshi, S., Otani, C., Dobroiu, A., Sato, H., Kawase, K., Shimizu, H. M., ... & Matsuo, H. (2006). Terahertz imaging with a direct detector based on superconducting tunnel junctions. *Applied physics letters*, *88*(20), 203503.

59. Drude, P. (1900). Zur elektronentheorie der metalle. *Annalen der Physik*, *306*(3), 566-613.
60. Nishi, Y., & Doering, R. (Eds.). (2000). *Handbook of semiconductor manufacturing technology*. CRC Press.
61. Ziegler, J. F. (Ed.). (2012). *Ion Implantation Science and Technology 2e*. Elsevier.
62. El-Kareh, B. (1994). *Fundamentals of semiconductor processing technology*. Springer Science & Business Media.
63. Griffin, P. B., Plummer, J. D., & Deal, M. D. (2000). Silicon VLSI technology: fundamentals, practice, and modeling. *1st. edition, Prentice Hall Inc*.
64. Sze, S. M. (2008). *Semiconductor devices: physics and technology*. John Wiley & Sons.
65. Wittmann, R. (2007). *Miniaturization problems in CMOS technology: Investigation of doping profiles and reliability*. na.
66. Ziegler, J. F., Biersack, J. P., & Littmark, U. (1985). The stopping and range of ions in matter, Vol. 1.
67. Hobler, G. (1988). *Simulation der Ionenimplantation in ein-, zwei-und dreidimensionalen Strukturen*. na.
68. Robles, S., Yieh, E., & Nguyen, B. C. (1995). Moisture resistance of plasma enhanced chemical vapor deposited oxides used for ultralarge scale integrated device applications. *Journal of the Electrochemical Society*, *142*(2), 580-585.
69. Ashok, A., & Pal, P. (2014). Growth and etch rate study of low temperature anodic silicon dioxide thin films. *The Scientific World Journal*, *2014*.
70. Wu, W. F., & Chiou, B. S. (1996). Optical and mechanical properties of reactively sputtered silicon dioxide films. *Semiconductor science and technology*, *11*(9), 1317.
71. Grove, A. S., Leistiko Jr, O., & Sah, C. T. (1964). Redistribution of acceptor and donor impurities during thermal oxidation of silicon. *Journal of Applied Physics*, *35*(9), 2695-2701.
72. Deal, B. E., Grove, A. S., Snow, E. H., & Sah, C. T. (1965). Observation of impurity redistribution during thermal oxidation of silicon using the MOS structure. *Journal of The Electrochemical Society*, *112*(3), 308-314.
73. Yoriume, Y. (1982). Deformation of silicon wafers by thermal oxidation. *Journal of the Electrochemical Society*, *129*(9), 2076-2081.
74. Thompson, M. J. (1984). Thin film transistors for large area electronics. *Journal of Vacuum Science & Technology B*, *2*(4), 827-834.
75. Pecora, A., Maiolo, L., Fortunato, G., & Caligiore, C. (2006). A comparative analysis of silicon dioxide films deposited by ECR-PECVD, TEOS-PECVD and Vapox-APCVD. *Journal of non-crystalline solids*, *352*(9), 1430-1433.
76. Bhatt, V., & Chandra, S. (2007). Silicon dioxide films by RF sputtering for microelectronic and MEMS applications. *Journal of micromechanics and microengineering*, *17*(5), 1066.
77. Kim, K. S., & Roh, Y. (2007). Silicon dioxide deposited by using liquid phase deposition at room temperature for nanometer-scaled isolation technology. *Journal of Korean Physical Society*, *51*, 1191.
78. Lewerenz, H. J. (1992). Anodic oxides on silicon. *Electrochimica Acta*, *37*(5), 847-864.

79. Duffek, E. F., Mylroie, C., & Benjamini, E. A. (1964). Electrode Reactions and Mechanism of Silicon Anodization in N-Methylacetamide. *Journal of the electrochemical society*, *111*(9), 1042-1046.
80. C. Panagopoulos and H. Badekas, "Growth of anodic SiO_2 films," Materials Letters, vol. 8, no. 6-7, pp. 212–215, 1989.
81. Kim, W. B., Matsumoto, T., & Kobayashi, H. (2009). Ultrathin SiO 2 layer with an extremely low leakage current density formed in high concentration nitric acid. *Journal of Applied Physics*, *105*(10), 103709-103709.
82. Hung, T. F., Wong, H., Cheng, Y. C., & Pun, C. K. (1991). A New Design of Anodic Oxidation Reactor for High-Quality Gate Oxide Preparation. *Journal of the Electrochemical Society*, *138*(12), 3747-3750.
83. Tiwald, T. E., Miller, A. D., & Woollam, J. A. (1998, November). Measurement of silicon doping profiles using infrared ellipsometry combined with anodic oxidation sectioning. In *AIP Conference Proceedings* (pp. 221-225). IOP INSTITUTE OF PHYSICS PUBLISHING LTD.
84. Jen, C. Y., & Richter, C. (2014). Doping Profile Recognition Applied to Silicon Photovoltaic Cells Using Terahertz Time-Domain Spectroscopy.
85. Jen, C. Y., & Richter, C. (2014). Sample Thickness Measurement with THz-TDS: Resolution and Implications. *Journal of Infrared, Millimeter, and Terahertz Waves*, *35*(10), 840-859.
86. Irvin, J. C. (1962). Resistivity of bulk silicon and of diffused layers in silicon. *Bell System Technical Journal*, *41*(2), 387-410.
87. Séverac, F., Cristiano, F., Bedel-Pereira, E., Lerch, W., Paul, S., & Kheyrandish, H. (2008). Evidence of the carrier mobility degradation in highly B-doped ultra-shallow junctions by Hall effect measurements. *Materials Science and Engineering: B*, *154*, 225-228.
88. Werner, S., Belledin, U., Kimmerle, A., Fallisch, A., Wolf, A., & Biro, D. (2010). Doping-and carrier concentration profile characterisation of highly phosphorus-doped emitters. In *Proceedings of the 25th European Photovoltaic Solar Energy Conference and Exhibition, Valencia, Spain* (pp. 1942-7).

Appendices

A. Flow chart illustrating new concept

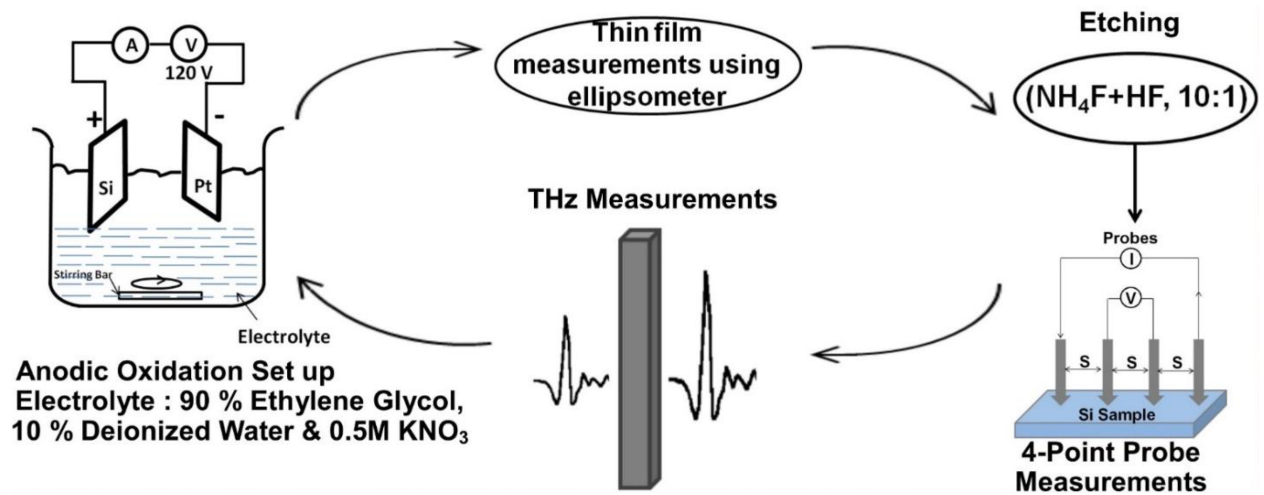

B. Derivation of complex transmission equation

The measurement period of our lab THz-TDS mainly covers the information from the first two peaks. Therefore, this equation is modified from the equation, which describes infinite peaks, to predict the complex transmission from the first two THz peaks. THz Transmission $\widetilde{E_T}$ of the first two peaks is considered as the superposition of $\widetilde{E_{T_1}} + \widetilde{E_{T_2}}$. In this case air scan is used as the reference.

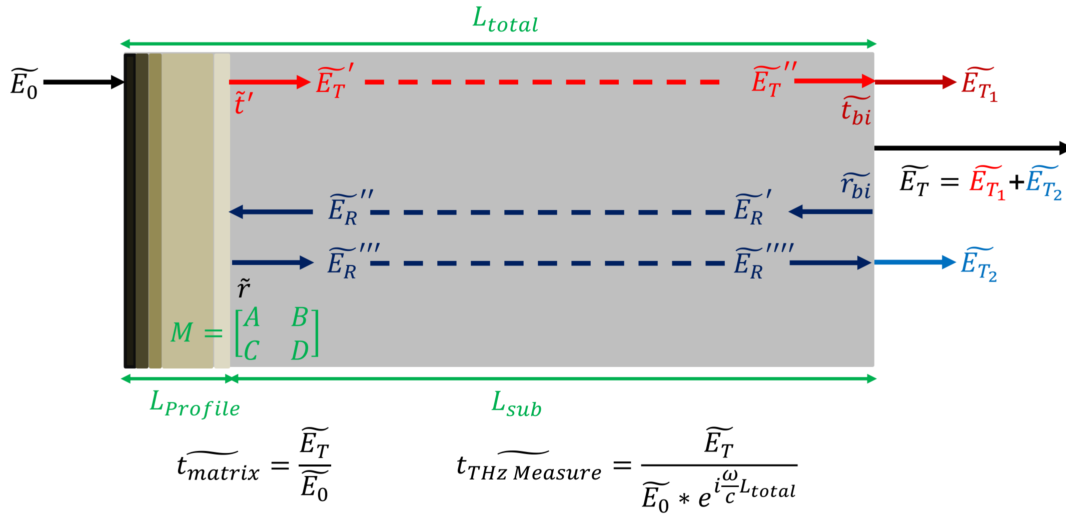

For the main peak transmission $\widetilde{E_{T_1}}$:

$$\widetilde{E_{T_1}} = \widetilde{t_{bi}}\widetilde{E_T}'' = \widetilde{t_{bi}}\widetilde{E_T}' e^{i\frac{n_{sub}\omega}{c}L_{sub}} = \tilde{t}'\widetilde{t_{bi}}\widetilde{E_0} e^{i\frac{n_{sub}\omega}{c}L_{sub}}$$

$$\Rightarrow \frac{\widetilde{E_{T_1}}}{\widetilde{E_0}} = \tilde{t}'\widetilde{t_{bi}} e^{i\frac{n_{sub}\omega}{c}L_{sub}} = \frac{2}{A+Bn_{sub}+C+Dn_{sub}} \frac{2n_{sub}}{n_{sub}+1} e^{i\frac{n_{sub}\omega}{c}L_{sub}}$$

$$\Rightarrow \widetilde{t_{THz_1}} = \frac{\widetilde{E_{T_1}}}{\widetilde{E_0} e^{i\frac{\omega}{c}L_{total}}} = \frac{2}{A+Bn_{sub}+C+Dn_{sub}} \frac{2n_{sub}}{n_{sub}+1} \frac{e^{i\frac{n_{sub}\omega}{c}L_{sub}}}{e^{i\frac{\omega}{c}L_{total}}}$$

For the 1st internal reflection peak $\widetilde{E_{T_2}}$:

$$\widetilde{E_{T_2}} = \widetilde{t_{bl}}\widetilde{E_R}'''' = \widetilde{t_{bl}}\widetilde{E_R}'''e^{i\frac{n_{sub}\omega}{c}L_{sub}} = \widetilde{t_{bl}}\tilde{r}\widetilde{E_R}''e^{i\frac{n_{sub}\omega}{c}L_{sub}} = \widetilde{t_{bl}}\tilde{r}\widetilde{E_R}'e^{i\frac{n_{sub}\omega}{c}L_{sub}}e^{i\frac{n_{sub}\omega}{c}L_{sub}}$$

$$= \widetilde{t_{bl}}\tilde{r}\widetilde{r_{bl}}\widetilde{E_T}''e^{i\frac{n_{sub}\omega}{c}L_{sub}}e^{i\frac{n_{sub}\omega}{c}L_{sub}}$$

$$= \widetilde{t_{bl}}\tilde{r}\widetilde{r_{bl}}\widetilde{E_T}'e^{i\frac{n_{sub}\omega}{c}L_{sub}}e^{i\frac{n_{sub}\omega}{c}L_{sub}}e^{i\frac{n_{sub}\omega}{c}L_{sub}} = \widetilde{t_{bl}}\tilde{r}\widetilde{r_{bl}}\tilde{t}'\widetilde{E_0}e^{i\frac{3n_{sub}\omega}{c}L_{sub}}$$

$$\Rightarrow \frac{\widetilde{E_{T_2}}}{\widetilde{E_0}} = \widetilde{t_{bl}}\tilde{r}\widetilde{r_{bl}}\tilde{t}'e^{i\frac{3n_{sub}\omega}{c}L_{sub}} = \frac{2n_{sub}}{n_{sub}+1}\frac{An_{sub}+Bn_{sub}-C-D}{An_{sub}+Bn_{sub}+C+D}\frac{n_{sub}-1}{n_{sub}+1}\frac{2}{A+Bn_{sub}+C+Dn_{sub}}e^{i\frac{3n_{sub}\omega}{c}L_{sub}}$$

$$\Rightarrow \widetilde{t_{THz_2}} = \frac{\widetilde{E_{T_2}}}{\widetilde{E_0}e^{i\frac{\omega}{c}L_{total}}} = \frac{2n_{sub}}{n_{sub}+1}\frac{An_{sub}+Bn_{sub}-C-D}{An_{sub}+Bn_{sub}+C+D}\frac{n_{sub}-1}{n_{sub}+1}\frac{2}{A+Bn_{sub}+C+Dn_{sub}}\frac{e^{i\frac{n_{sub}\omega}{c}L_{sub}}}{e^{i\frac{\omega}{c}L_{total}}}$$

$$\therefore t_{\widetilde{THz_Measure}} = \widetilde{t_{THz_1}} + \widetilde{t_{THz_2}}$$